

**NASA TECHNICAL  
MEMORANDUM**

**NASA TM X-52245**

GPO PRICE \$ \_\_\_\_\_

CFSTI PRICE(S) \$ \_\_\_\_\_

Hard copy (HC) 2.50

Microfiche (MF) .75

# 853 July 85

NASA TM X-52245

FACILITY FORM 602  
N66 39975  
(ACCESSION NUMBER)  
84  
(PAGES)  
TMX-52245  
(NASA CR OR TMX OR AD NUMBER)

(THRU)  
7  
(CODE)  
15  
(CATEGORY)

**EXPERIMENTAL AND THEORETICAL  
STUDY OF THE VISCOSEAL**

by John Zuk, L. P. Ludwig, and R. L. Johnson  
Lewis Research Center  
Cleveland, Ohio

TECHNICAL PAPER proposed for presentation at  
meeting on Development of Turbulent-Flow Bearings and  
Seals for Process-Fluid Lubricated Turbomachinery  
Latham, New York, November 1, 1966

**EXPERIMENTAL AND THEORETICAL STUDY OF THE VISCOSEAL**

**by John Zuk, L. P. Ludwig, and R. L. Johnson**

**Lewis Research Center**

**Cleveland, Ohio**

**TECHNICAL PAPER proposed for presentation at**

**Meeting on Development of Turbulent-Flow Bearings and  
Seals for Process-Fluid Lubricated Turbomachinery**

**Latham, New York, November 1, 1966**

**NATIONAL AERONAUTICS AND SPACE ADMINISTRATION**

# EXPERIMENTAL AND THEORETICAL STUDY OF THE VISCOSEAL

by John Zuk, L. P. Ludwig, and R. L. Johnson

Lewis Research Center

National Aeronautics and Space Administration

Cleveland, Ohio

## SUMMARY

Experimental studies were conducted on pressure patterns, gas ingestion, and sealing capacity of viscoseals. Oil, water, and liquid sodium were used as the sealed fluids. Results indicated that when the groove-land pairs connected directly with the pressurized cavity (without an intermediate circumferential groove), an end effect, or ineffective seal length, was evidenced by a sharp decay of pressure along the land leading edge. Results also disclosed that a helically grooved rotor viscoseal has increasing gas ingestion rates with increasing Reynolds number when the viscoseal liquid interface becomes unstable. However, if the helical grooves are in the housing (smooth rotors), gas ingestion could be eliminated by increasing Reynolds number. Secondary grooves on viscoseal land areas improved sealing capacity and reduced power absorption. Sodium was sealed at 300<sup>0</sup> to 625<sup>0</sup> F with negligible liquid loss.

From a theoretical analysis, a set of two-dimensional equations (that includes both convective inertia and viscous forces) were formulated for a quasi-two-dimensional flow field in parallel groove geometries which can be used as a mathematical model for the viscoseal. The mathematical model consisted of an infinite smooth flat plate moving relative to a fixed infinite parallel groove-ridge surface with the clearance filled with an incompressible, homogeneous, Newtonian fluid. A modified Reynolds number evolved that is based on a groove-ridge characteristic length parallel to

the smooth plate velocity vector. Application of the modified Reynolds number to published experimental results reveals that a significant improvement (previously attributed to onset of turbulence) in bearing number or sealing coefficient occurred when the modified Reynolds number was near unity; therefore, it is argued that the strong influence of convective inertia, and not turbulence, is the main cause of this improvement. For this reason a turbulent flow model should include the convective inertia effects. The consideration of convective inertia effects reveals that fluid density  $\rho$ , aspect ratio  $b/h_0$ , and number of groove-ridge pairs  $N$  are additional parameters of pressure generation dependence that are not revealed by creeping flow analyses. The analysis presented herein provides a unified approach which was previously covered by the creeping flow and the semiempirical turbulent flow analyses. No restriction was placed on the net flow; therefore, the analysis applies equally to hydrodynamic seals, bearings, and pumps. An arbitrary groove-ridge shape is also permissible in solving equations. Consideration of convective inertia effects suggests the principle of viscoseal axial pressure generation and attainment of zero leakage.

## INTRODUCTION

The viscoseal is a special case of a general class of parallel groove geometries which have many potential applications for use as pressure generation devices. For example, the parallel groove has been applied in spiral groove thrust bearings (ref. 1), spherical and conical spiral groove bearings (ref. 1), helical groove pumps (ref. 2), as well as helical groove seals (viscoseal, ref. 3).



The visco seal is potentially useful for sealing liquid metals, such as mercury, potassium, and sodium, in space electric-power generation systems that require 1 to 3 years of unattended operation and near zero leakage (refs. 4 and 5). As pointed out in references 5 and 6, the visco seal has inherent reliability and long life because of the absence of solid surfaces in rubbing contact.

To date, analyses of parallel groove geometry have been limited to creeping flow solutions where convective inertia effects have been neglected. Convective inertia is the fluid mass acceleration due to a spatial velocity change, for example, a change in velocity due to an obstacle in the flow path. This is contrasted to an inertia effect caused by a temporal velocity change, for example, a variation in velocity at a point in a bearing due to shaft runout (which is a function of time). The creeping flow analysis is restricted to flows where the modified Reynolds number (see DISCUSSION) is much less than 1; that is,

$$Re = Re_L \left( \frac{c}{L} \right)^2 \ll 1$$

or

$$Re \lesssim 0.01$$

where

$$Re_L = \frac{UL}{\nu} = \frac{\rho UL}{\mu}$$

$$\frac{c}{L} < 1$$

Creeping flow analyses for pumps, screw extruders, seals, and thrust and journal bearings have been published by many authors (e. g.,

refs. 1 to 26). Appendix C contains an outline and discussion of the published creeping flow solutions. The main criticism of the creeping flow solution (generally used in the laminar flow regime) is that its validity is restricted to Reynolds numbers below most engineering applications.

A number of semiempirical and turbulent flow formulations have been devised (refs. 4, 18, 27, and 28) for operation in a regime designated as turbulent, but they neglect the convective inertia terms which are important physically. The main criticism of these semiempirical analyses and turbulent flow model is that the existence of the turbulent regime is assumed. Turbulence, however, may not be necessary to explain reported experimental results and may not even exist. Even if turbulence does exist, convective inertia effects are thought to be far more significant. Kettleborough (ref. 29) numerically analyzed the slider bearing with inertia, turbulent, and viscous terms considered. When inertia only was considered, the results were in qualitative agreement with published (turbulent-attributed) slider bearing experimental results. Kettleborough concluded that the turbulence term did not appear to greatly affect the operation of the slider bearing.

Golubiev (ref. 24) applied centrifugal pump similarity laws to the helical groove seal (including operation where the rotor and housing are both grooved). This case considers an inviscid fluid (viscous forces neglected) whereby the pressure generation is found from Bernoulli's equation modified by a geometric constant, where  $\Delta P$  varies as the square of the velocity. The viscous force cannot be neglected for two reasons: (1) the viscous force causes fluid motion, and (2) the viscous force contributes to maintaining the generated pressure gradient. Unfortunately, the creeping

flow optimum geometry has been extended to be valid for operation beyond the creeping flow regime. Since the convective change is the main driving force, a complete reevaluation of the optimum geometry including the groove-ridge shape must be investigated before conclusions on visco-seal performance can be made. Experiments show that the optimum geometry changes for flow beyond the creeping flow regime (ref. 27).

Several authors (refs. 20 and 21) reported that the viscoseal had a certain ineffective length at the high-pressure end of the seal. This has been called the end effect, and it has been suggested (ref. 20) that this ineffective rotor length be subtracted from the calculated wetted-seal length in order to compare theory and experiment. Muijderman (ref. 1) derived theoretical pressure patterns for the spiral groove geometry on plane surfaces and developed an analytical method of correcting for the end effect. However, pressure patterns in the viscoseal and end-effect alterations of these patterns have not been determined experimentally. Existing experimental data consists of average pressure measurements from which the existence of an end effect is deduced.

Gas ingestion from the low-pressure to the high-pressure end of the seal is reported to have occurred when sealing potassium (ref. 4) and when sealing water (refs. 5 and 27). Although this gas ingestion characteristic may present no problem with a vacuum on the low-pressure end, it is highly undesirable in other potential applications because of contamination and/or detrimental effect on sealing capacity. Reference 24 reports that in attempting to seal a liquid, the viscoseals (combining helical grooves in rotor and housing) worked on an air-liquid emulsion, and reference 25 reports that viscoseals (helical grooves on shaft)

operate with a mixture of oil and gas. These modes of operation could be due to gas ingestion. Leakage observations reported in reference 21 on "seal breakdown" and in reference 4 on "secondary leakage" could result from gas ingestion into a closed cavity.

The objectives of these studies were:

- (1) Study experimentally the pressure patterns in the viscoseal with particular emphasis on the pattern near the seal end (end effect)
- (2) Investigate experimentally gas ingestion and sealing capacity of the viscoseal
- (3) Develop a physical flow model for a theoretical analysis of the viscoseal

The data and analysis contained herein is covered in detail by the authors' papers (refs. 5, 6, and 30).

#### SYMBOLS

$a$	ridge or land width
$a'$	ridge or land width parallel to viscoseal centerline
$\vec{a}$	acceleration vector
$b$	groove width
$b'$	groove width parallel to viscoseal centerline
$C$	specific heat of fluid
$C_p$	specific heat of fluid at constant pressure
$c$	clearance between ridge and smooth flat plate, or radial clearance
$\hat{e}_n$	unit normal directed toward axis
$\hat{e}_t$	unit normal tangent to trajectory
$F_x$	body force in x-direction
$F_y$	body force in y-direction

$F_z$	body force in z-direction
$G$	dimensionless factor, function of helical geometry
$g$	acceleration of gravity
$h_o$	step or edge height (or groove depth)
$k$	thermal conductivity of fluid
$L$	characteristic length, length of groove-ridge pair in smooth plate
	relative velocity vector direction
$L'$	axial length, normal to plate velocity
$N$	number of helix starts
$n$	integer
$\Delta P$	pressure differential
$P^*$	static pressure at reference state
$P_c$	static cavity pressure
$Pr$	Prandtl number
$Q$	net volume flow rate
$Q^*$	heat source energy
$Q_\eta$	volume flow rate normal to plate relative velocity direction
$Q_\xi$	volume flow rate in plate relative velocity direction
$q$	fluid velocity in x-z plane
$R$	radius of rotor
$Re$	Reynolds number
$Re^*$	modified or reduced Reynolds number
$T^*$	temperature at reference state
$t$	time
$U$	smooth flat-plate velocity or rotor surface speed
$u$	velocity in x-direction

$V$	characteristic velocity in the y-direction
$\vec{V}$	fluid velocity vector
$V_{p,x}$	pressure flow velocity in x-direction
$V_{p,z}$	pressure flow velocity in z-direction
$v$	velocity in y-direction
$w$	velocity in z-direction
$x$	coordinate along ridge-groove
$y$	coordinate across film (between plates)
$z$	coordinate across ridge-groove
$\alpha$	angle between relative velocity direction and parallel groove- ridges or helix angle
$\zeta$	film height
$\eta$	coordinate normal to plate relative velocity vector
$\theta$	temperature ratio = $\frac{T - T_S}{T_M - T_S}$
$\Lambda$	bearing number
$\lambda G$	empirical sealing parameter (defined in ref. 5)
$\mu$	absolute viscosity of fluid
$\nu$	kinematic viscosity of fluid
$\nu^*$	kinematic viscosity of fluid at reference state
$\xi$	coordinate in direction of plate relative velocity vector
$\rho$	density
$\rho^*$	density at reference state
$\sigma$	shape parameter
$\Phi$	dissipation function
$\varphi$	angle traversed in polar plane

$\nabla$  vector differential operator Del or Nabla

$\nabla^2$  Laplacian operator

Subscripts:

c based on clearance or film thickness

g groove

L based on characteristic length

M moving surface

n normal direction

r ridge or land

S stationary surface

t tangential direction

z across ridge-groove

$\epsilon$  plate relative velocity direction

$\eta$  normal to plate velocity direction (axial length)

## APPARATUS AND PROCEDURE

### Experimental Study of Pressure Patterns

Figure 1 shows a schematic drawing of the experimental apparatus and viscoseal assembly used to study end effects and pressure patterns. The rotor of the viscoseal is attached to the power input shaft which is supported by externally pressurized gas journal bearings. Axial thrust due to sealed fluid cavity pressure against the rotor is resisted by the externally pressurized gas thrust bearing. The power input shaft is driven by a variable-speed electric drive and step-up transmission. A magnetic pickup monitors the shaft speed. The viscoseal housing is attached to a support shaft and roller bearing assembly, which permits axial adjustment. A pump pressurizes the seal housing cavity and circu-

lates a cooling fluid flow from the reservoir, through a heat exchanger, to the test cavity and then back to the reservoir. This cooling flow is necessary to control fluid film temperature in the viscoseal. The steel rotors have a centerline average surface finish of  $20 \times 10^{-6}$  inch and are mounted within 0.0002 inch of the total indicator reading. The viscoseal housing is constructed from acrylic plastic and contains thermocouples and pressure taps as shown in figure 2. Pressure taps, in a line parallel to the axis, are located at groove edges and midland and midgroove positions; pressure taps are also located near both edges along one groove. Two sets of four pressure taps ( $90^\circ$  apart) were used to align the housing with respect to the rotor within 0.0004 inch as determined by calibration. Thermocouples were located flush with the bore and groove root in a line parallel to the axis and at each midgroove and midland position. Figure 2 also gives the groove dimensions used in this evaluation. The housing had a 2.001-inch bore and a  $14\frac{1}{2}^\circ$  helix angle. Groove widths of 0.19 inch and land widths of 0.13 inch were provided by using five helix grooves (five starts). These geometric proportions, which are based on the optimum relations given by reference 19, included a 0.015 inch groove depth and a rotor radial clearance of 0.005 inch.

The kinematic viscosity-temperature relations for the mineral oil used were found to be the same before and after use in the test. These values can be found in table I.

#### Experimental Study of Gas Ingestion and Sealing Capacity

In studies on sealing water (fig. 3), the water pressure and flow to the pressurized cavity (at the viscoseal high-pressure end) were controlled by throttling valves on the inlet and outlet water lines. This arrangement



provided temperature control of the sealed fluid. A transparent housing permitted visual observations on the rate of gas flow out of the pressurized cavity; and, in studies on grooved rotors, a stroboscope permitted observations of the gas ingestion process in the rotating grooves.

Figure 4 is a diagrammatic sketch of the experimental apparatus used for evaluating viscoseals in sodium. The temperature was maintained by a furnace (resistance heaters) surrounding the viscoseal housing. The temperature was monitored by thermocouples attached to the seal housing outer diameter and by one thermocouple submerged in the sodium in the pressurized cavity.

The enclosure surrounding the viscoseal assembly is pressurized with argon (after prior evacuation) to slightly above ambient to insure exclusion of air. Prior to the introduction of liquid sodium, the input shaft is set at some fixed speed. Sodium is introduced by pressurizing the reservoir and venting the leak detector tank (see sodium supply system in fig. 5). The sodium first fills the pressurized cavity (viscoseal high-pressure end) and then is allowed to fill the leak detector tank to a predetermined level. The leak detector tank float displacement is monitored by recording the differential transformer output that is produced by the transformer core attached to the top of the float. Thermocouples placed at different levels in the tank provide calibration during the filling process.

By holding the reservoir temperature at 220<sup>0</sup> F, a low degree of oxide solubility was maintained. The 20-micron filter (stainless steel) inside the tank allowed 220<sup>0</sup> F filtration. A second filter external to the reservoir (5 microns) provides additional filtering at approximately 300<sup>0</sup> F. Sodium is partially removed from the system by pressurizing the leak detector and

forcing the sodium back into the reservoir. By alternately filling the system and then partially returning the sodium to the reservoir, the sodium can be recirculated and refiltered. This recirculation provides a hot flush or cleaning action on the viscoseal assembly before a run. (All transfer lines and the test section are held at 300<sup>0</sup> to 500<sup>0</sup> F during this recirculation process.) For all sodium studies the leak detector tank was held at 300<sup>0</sup> F, and any seal leakage resulted in a drop of liquid level and float position. Gas ingestion into the pressurized cavity was indicated by a rise in sodium level in the leak detector.

Sealing capacity, when sealing sodium, was obtained by increasing cavity pressure until the leak detector indicated leakage. Line thermocouple readings were also found to be sensitive leak indicators. Viscoseal geometries employed in this evaluation are shown in table II. The geometry near the optimum (derived in ref. 19) was taken as the basis for comparison, and is listed in the first row of table II as geometry 1. Secondary grooves were added to the lands of this basic geometry to form the second geometry evaluated. For the third geometry, a ratio of groove to land width of 1.90 was selected; and for the fourth geometry, secondary grooves were added to geometry 3. Geometry 5 is the internally grooved housing having the same groove dimensions as geometry 1. The rotor outer diameters were 1.993 inches, and the housing bores were 2.001 inches.

## EXPERIMENTAL RESULTS AND DISCUSSION

### Pressure Patterns

Figure 6 shows an experimentally determined pressure pattern in a viscoseal composed of an internal helically grooved housing and a smooth

rotor arrangement. In a plane orthogonal to the rotor centerline, the pressure increases across the groove (from point A to B) in the direction of rotor rotation and decreases across the land (from point B to C). The increase and decrease in pressure repeat for each groove-land pair and produce a saw-tooth pressure profile in the orthogonal plane. The pressure increases from the low-pressure end (plane 3) to the high-pressure end (plane 1), and the pressure pattern has a helical twist corresponding to the helical grooves. (For a rotating grooved shaft this pressure pattern would be rotating.)

The pressure gradients in the planes orthogonal to the rotor centerline are essentially linear for axial positions not influenced by the end effects. Figure 7 shows typical experimental results. These pressure profiles are the same as those for the orthogonal planes shown in figure 6 except that a single groove-land pair is unwrapped to form a plane figure. (Neglecting curvature is not a significant error since the ratio of rotor radius to groove depth is 65 to 1.)

In these orthogonal planes, the ratio of pressure to cavity pressure  $P/P_c$  increases linearly over the groove and then decreases linearly over the land. This linear relation was found to hold to the maximum test speed of 6000 rpm, which produced a modified Reynolds number ( $Re^*$ ) of 0.25.

#### End Effect

When the helical grooves connect directly with the pressurized cavity, the pressure developed along the land leading edge decays sharply near the high-pressure end of the seal. Typical results are shown in figure 8 for 1000 and 6000 rpm. The pressure pattern at the end was essentially the same for the speed range investigated (1000 to 6000 rpm) except

that the results for 5000 rpm (not shown) and 6000 rpm start to show a slight shortening of the end-effect length. This shortening is probably due to convective inertia effects. In all cases, the end-effect axial length was approximately equal to one-half the axial groove width. This suggests that end-effect length could be taken to one-half groove width without significant error. The pressure decay within the groove is due to the equalization of the land leading- and trailing-edge pressure, since a common pressure must exist in the cavity.

### Gas Ingestion and Sealing Capacity Observations

#### When Sealing Water

Grooved housing. - The series of photographs in figure 9 shows the gas ingestion process when sealing water with a grooved housing and smooth outer diameter rotor. At a modified Reynolds number ( $Re^*$ ) of 1.75 (2000 rpm), no gas ingestion is evident, the water film is clear, the interface is stable, and the scavenging length is nonwetted.

At  $Re^* = 2.58$  (3000 rpm) the film had large gas pockets, gas was ingested as evidenced by air bubbles passing out of the transparent vent line, and the sealing capacity (parameter,  $\lambda G$ ) was lower than that at  $Re^* = 1.75$  (2000 rpm). Various degrees of gas ingestion and film rupture are evident for  $Re^* = 3.50$  (4000 rpm) to 6.10 (7000 rpm). At  $Re^* = 7.00$  (8000 rpm), no detectable gas ingestion rate was evident, and gas ingestion was not detectable from  $Re^* = 7.00$  (8000 rpm) to the highest speed evaluated, which gave  $Re^* = 10.84$  (12 000 rpm). At  $Re^* = 7.00$  and above, the seal wetted length had two distinct regions (fig. 10(f)): a gas-liquid region, and a region of homogeneous liquid at the high-pressure end.

Between  $Re^* = 3.5$  and  $6.10$ , it was observed that the bubble size progressively decreased when moving from the low-pressure end to the high-pressure end. It is probably that with longer seal lengths the corresponding higher pressures would reduce the bubble size sufficiently to allow escape over the lands, and thus gas ingestion would be eliminated. It was observed that concentricity of rotor and housing markedly affect gas ingestion occurrence.

Grooved rotor. - In a series of visual observations using a grooved rotor, the gas ingestion started at  $Re^* = 1.9$  and increased in rate with increasing Reynolds number (maximum investigated,  $Re^* = 10.84$ ). Below  $Re^* = 1.9$  the liquid-to-gas interface was stable and no gas ingestion was observed.

Gas ingestion mechanism. - These observed gas ingestion characteristics of the grooved rotor and the grooved housing are illustrated in figure 10. The probable mechanism producing the difference between the gas ingestion process of the grooved rotor as compared with that of the grooved housing is illustrated in figure 11. For the grooved housing, when the centrifuge action on the liquid becomes great enough, the gas bubbles are displaced to the rotor surface and pass over the lands. Therefore, the bubbles are not pumped to the high-pressure end. For the grooved rotor, the centrifugal action on the liquid forces the gas bubbles into the grooves; therefore, the bubbles are pumped to the high-pressure end of the seal.

When a viscoseal is ingesting gas, the axial pressure gradient is non-linear and increases as the liquid-to-gas volume ratio increases in the direction toward the high-pressure end. For no gas ingestion, the axial pressure gradients are linear as shown in figure 8, which contains data

on sealing oil. As shown in figure 12, gas ingestion results in nonlinear pressure gradients (increasing slope with increasing liquid-gas volume), which are significantly different from the gradients shown in figure 8.

Leak rate. - In both viscoseal combinations (grooved housing and grooved rotor) water was sealed, with no detectable leakage. It was observed that, although gas ingestion reduced the sealing capacity  $\lambda G$ , effective sealing of the water was maintained.

#### Results of Sodium Sealing Studies

Grooved housing. - In sealing sodium, the grooved housing did not ingest gas (fig. 13) for concentric alignment (0.005 in. F.I.R.) over the range investigated ( $Re^* = 8.66$  to  $50.5$ ) and for pressures ranging from 2 to 100 psig. The sensitivity of the leak detector to measure gas ingestion rate was estimated to be 0.50 cubic centimeter per hour. It was observed that nonconcentricity leads to gas ingestion, but this situation was not investigated.

Grooved rotor. - The grooved rotor started to ingest gas at  $Re^* = 10$ , and the rate increased with increasing Reynolds number, as shown in figure 13. This ingestion characteristic is similar to that observed when sealing water with the grooved rotor.

Gas ingestion into closed cavity. - In sealing sodium, gas ingestion was readily observed by monitoring the liquid level in the leak detector. As shown in figure 14, a straight line on the oscillograph paper indicated no gas ingestion, no leakage, and thermal equilibrium. When gas ingestion occurred, the liquid level line showed an upward trend, the slope of which is the ingestion rate. As gas ingestion proceeds, the gas bubble in the pressurized cavity increases in size (fig. 14(a)), and when the size

increases to the rotor outer diameter, the gas flows back out the annulus formed by the rotor and housing. This causes a decrease in bubble size and a sharp drop in the leak detector readout trace. If the interface is far enough away from the seal low-pressure end, the liquid will be scavenged back within the nonwetted length, and no loss of liquid will occur. The ingestion process will begin again and the net result is a saw-toothed trace, each sharp drop indicating gas blowback. If the interface is sufficiently close to the seal end, liquid loss will occur, and the leak detector readout will show a saw-toothed trace with a downward trend, which represents a liquid loss at each blowout (fig. 14(c)). This latter action may be the "seal breakdown" phenomenon reported in reference 21 and the "secondary leakage" phenomenon reported in reference 4. (In sealing water, the repeating bubble growth and subsequent seal blowout was visually observed by means of a transparent housing.)

Sealing capacity. - The grooved housing had a higher sealing capacity (higher sealing parameter,  $\lambda G$ ) than the grooved rotor. The comparison is given in figure 15, which gives the sealing parameter  $\lambda G$  as a function of Reynolds number based on  $c$  ( $Re_c$ ). The difference between the value of  $\lambda G$  for the grooved housing and the value for the grooved rotor was attributed to the difference in gas ingestion characteristics. The grooved rotor operates with a gas-liquid mixture along the full wetted length similar to that shown in figures 9(b) to (e); the grooved housing operates with a homogeneous liquid at the high-pressure end of the seal and a gas-liquid mixture at the low-pressure end similar to that shown in figure 9(f).

Figures 16(a) and (b) show the sealing parameter  $\lambda G$  as a function of Reynolds number ( $Re_c$ ) for groove configurations of five- and ten-helix

starts (see table II) with and without secondary grooves on the lands. In both cases, a higher sealing coefficient was obtained through the use of secondary grooves. Secondary grooves also operate at lower power absorption levels for equal sealing capacity, as was determined by the amount of heating power required to maintain operating temperature. This lower power absorption is due to less land area as compared with the land area of the seals without secondary grooves.

Sodium was sealed for pressures ranging from 2 to 100 psig with negligible leakage loss. The operating range was within Reynolds numbers ( $Re^*$ ) of 8.66 to 50.5, and the fluid temperature was in the range  $300^{\circ}$  to  $625^{\circ}$  F. The maximum length of any one run was 8 hours and accumulated testing time amounted to 50 hours for 10 runs. The oxygen content of the sodium for the 10 runs varied between 50 to 95 parts per million, as determined by the analytical method described in reference 31.

## THEORETICAL ANALYSIS OF THE VISCOSEAL

### Basic Model

The rectilinear Cartesian coordinate system was selected for mathematical tractability. A parallel groove-ridge plate geometry with a smooth flat plate moving relative to the parallel groove-ridge plate, both of infinite horizontal extent, was chosen as the basic model (see fig. 17).

Conceptually this model can be thought of as an infinitely long smooth rotor with a very large diameter and a concentric grooved housing. Actually this infinite grooved plate model is the limiting case of a helical grooved cylinder where  $R \rightarrow \infty$  or  $c \rightarrow 0$ . If  $c/R \lesssim 0.01$ , this model should give a good qualitative picture of the flow field and pressure generation and significant trends for optimum geometry. (See argument in



appendix A.) For example, a practical geometry is a 2-inch-diameter rotor with a 0.005-inch concentric clearance,  $c/R = 0.005$ .

The clearance between the infinite plates is filled with any incompressible fluid, and it should be noted that for this infinite horizontal extent case there are no end effects (in practical engineering design, of course, end effects must be accounted for). Since experiments at Lewis show that the end effect zone decreases with increasing rotor speed and also that it is less than a groove width, this analysis should be valid in the bulk of the homogeneous fluid (see figs. 18 and 19).

In the flat-plate case, the boundary conditions on a groove-ridge plate in motion are constant; however, it will be advantageous to have the smooth flat plate move relative to the grooved flat plate. This will eliminate the temporal inertia terms and reduce the subsequent independent variables by one.

A word of caution for extension of the results to a case where the groove-ridge pairs on a finite shaft are rotating relative to a fixed smooth housing. The boundary conditions are different when the smooth housing is stationary and the grooved rotor is moving, and when the housing is grooved and the rotating shaft is smooth. When the rotor is grooved, the surface speed is different at each point along the step or edge of the moving boundary. Thus this analysis should be more valid for a smooth rotor and grooved fixed housing (from ref. 5 the grooved housing appears to be the desired mode of operation) with a large radius of curvature and/or small clearance.

When referring to figure 17, it is noted that by the choice of coordinate system the groove-ridge pairs appear only in the  $y, z$ -plane. Later it will

be shown that this choice of coordinate system will be necessary to reduce the analysis to a two-dimensional problem for the quasi two-dimensional flow field. It should also be noted that the drag force has been resolved into its components in this coordinate system and there is no equilibrium of forces in the z-direction with inertia (nonlinear) effects neglected.

### BASIC EQUATIONS

The Navier-Stokes equations for a homogeneous, incompressible, laminar, Newtonian fluid are the following (see ref. 32):

x-direction:

$$\rho \frac{Du}{Dt} = F_x - \frac{\partial P}{\partial x} + \mu \left( \frac{\partial^2 u}{\partial x^2} + \frac{\partial^2 u}{\partial y^2} + \frac{\partial^2 u}{\partial z^2} \right) \quad (1)$$

y-direction:

$$\rho \frac{Dv}{Dt} = F_y - \frac{\partial P}{\partial y} + \mu \left( \frac{\partial^2 v}{\partial x^2} + \frac{\partial^2 v}{\partial y^2} + \frac{\partial^2 v}{\partial z^2} \right) \quad (2)$$

z-direction:

$$\rho \frac{Dw}{Dt} = F_z - \frac{\partial P}{\partial z} + \mu \left( \frac{\partial^2 w}{\partial x^2} + \frac{\partial^2 w}{\partial y^2} + \frac{\partial^2 w}{\partial z^2} \right) \quad (3)$$

The Eulerian or spatial derivative is  $D/Dt$ , which is composed of the local acceleration (temporal velocity change) and the convective acceleration (spatial velocity change):

$$\frac{D}{Dt} = \underbrace{\frac{\partial}{\partial t}}_{\text{Local, unsteady, or nonstationary acceleration}} + \underbrace{u \frac{\partial}{\partial x} + v \frac{\partial}{\partial y} + w \frac{\partial}{\partial z}}_{\text{Convective acceleration}}$$

The incompressible continuity equation is

$$\frac{\partial u}{\partial x} + \frac{\partial v}{\partial y} + \frac{\partial w}{\partial z} = 0 \quad (4)$$

The incompressible energy equation with constants  $C$  and  $k$  and neglecting compression work  $DP/Dt$  (ref. 32)

$$\rho g C \frac{DT}{Dt} = k \left( \frac{\partial^2 T}{\partial x^2} + \frac{\partial^2 T}{\partial y^2} + \frac{\partial^2 T}{\partial z^2} \right) + \mu \Phi + Q^* \quad (5)$$

where  $\Phi$  is the dissipation function

$$\begin{aligned} \Phi = 2 \left[ \left( \frac{\partial u}{\partial x} \right)^2 + \left( \frac{\partial u}{\partial y} \right)^2 + \left( \frac{\partial w}{\partial z} \right)^2 \right] &+ \left( \frac{\partial v}{\partial x} + \frac{\partial u}{\partial y} \right)^2 + \left( \frac{\partial w}{\partial y} + \frac{\partial v}{\partial z} \right)^2 \\ &+ \left( \frac{\partial u}{\partial z} + \frac{\partial w}{\partial x} \right)^2 - \frac{2}{3} \left( \frac{\partial u}{\partial x} + \frac{\partial v}{\partial y} + \frac{\partial w}{\partial z} \right)^2 \end{aligned}$$

The assumptions for this analysis are as follows:

(1) For steady flow,

$$\frac{\partial u}{\partial t} = \frac{\partial v}{\partial t} = \frac{\partial w}{\partial t} = 0$$

(2) For no body forces,

$$F_x = F_y = F_z = 0$$

This means there are no electromagnetic fields present and gravitational effects are negligible.

(3) Isothermal and equal temperature plate surface conditions are assumed.

(4) Viscous (frictional) heating is negligible. Therefore, the thermo-physical properties are constant. This appears to be a good assumption for order 10 (water) and smaller (liquid metals) Prandtl number  $Pr$  fluids:

$$Pr = \frac{C_p \mu}{k}$$

In experimental setups there is an inherent unsteadiness due to vibrations, shaft runout, and eccentricity of rotor with respect to housing and misalignment. These factors will influence the degree of correlation between the analytical and experimental results.

The conservation of momentum and mass equations were nondimensionalized and a formal ordering procedure was used to determine the relative magnitude of the terms. Consequently, in a formal way the negligible terms were found (see appendix A).

An important parameter, the modified or reduced Reynolds number, was found:

$$Re^* = Re_L \left( \frac{c}{L} \right)^2 = Re_c \left( \frac{c}{L} \right) \quad \text{if } c/L < 1$$

This modified Reynolds number gives the relative magnitude of the inertia forces to the viscous forces; that is,

$$Re^* = \frac{\text{Inertia forces}}{\text{Viscous forces}}$$

Thus, inertia forces can be neglected only if  $Re^* \lesssim 0.01$ .

After the formal ordering procedure (see appendix A), the three-dimensional flow field equations are as follows:

Conservation of momentum:

$$u \frac{\partial u}{\partial x} + v \frac{\partial u}{\partial y} + w \frac{\partial u}{\partial z} = - \frac{1}{\rho} \frac{\partial P}{\partial x} + \nu \frac{\partial^2 u}{\partial y^2} \quad (\text{x-direction}) \quad (6)$$

$$\frac{\partial P}{\partial y} \cong 0 \quad (\text{y-direction}) \quad (7)$$

$$u \frac{\partial w}{\partial x} + v \frac{\partial w}{\partial y} + w \frac{\partial w}{\partial z} = - \frac{1}{\rho} \frac{\partial P}{\partial z} + \nu \left( \frac{\partial^2 w}{\partial y^2} + \frac{\partial^2 w}{\partial z^2} \right) \quad (\text{z-direction}) \quad (8)$$

Conservation of mass:

$$\frac{\partial u}{\partial x} + \frac{\partial v}{\partial y} + \frac{\partial w}{\partial z} = 0 \quad (4)$$

Fully developed flow is assumed in the x-direction. This means that  $\bar{V}$  and  $\partial P / \partial x$  are not functions of  $x$  and that the pressure gradient in the x-direction (parallel to the groove) is a constant (verified experimentally in ref. 5). In figure 18, it is observed that this assumption is valid only where the average pressure profile at the ridge leading or trailing edges in the axial direction is linear. Gas ingestion results in a nonlinear profile (see figs. 18 and 19).

With the assumption of fully developed flow along the groove-ridge direction (x-direction), the flow field equations become two-dimensional:

$$v \frac{\partial u}{\partial y} + w \frac{\partial u}{\partial z} = - \frac{1}{\rho} \frac{\partial P}{\partial x} + \nu \frac{\partial^2 u}{\partial y^2} \quad \text{where} \quad \frac{\partial P}{\partial x} = \text{constant} \quad (9)$$

$$\frac{\partial P}{\partial y} \cong 0 \quad (10)$$

$$v \frac{\partial w}{\partial y} + w \frac{\partial w}{\partial z} = - \frac{1}{\rho} \frac{\partial P}{\partial z} + \nu \left( \frac{\partial^2 w}{\partial y^2} + \frac{\partial^2 w}{\partial z^2} \right) \quad (11)$$

Conservation of mass:

$$\frac{\partial v}{\partial y} + \frac{\partial w}{\partial z} = 0 \quad (12)$$

The boundary conditions for an arbitrary shaped groove-ridge geometry (see fig. 20) are:

(1)

$$\left. \begin{aligned} v &= 0 \\ u &= U \cos \alpha \\ w &= -U \sin \alpha \end{aligned} \right\} \text{ at } y = 0$$

(2)

$$u = v = w = 0 \quad \text{at } y = h(z)$$

For example, when  $h(z)$  is a rectangular groove-ridge pair the boundary condition is:

$$u = v = w = 0 \quad \text{at } c \leq y \leq c + h_0 \quad (\text{on side of groove})$$

$$u = v = w = 0 \quad \text{at } y = c \quad (\text{on ridge})$$

$$u = v = w = 0 \quad \text{at } y = c + h_0 \quad (\text{on groove root})$$

(3) Periodicity of groove-ridge pairs at the clearance interface.

For  $0 \leq y < h(z)$

$$v(0, y) = v(L \sin \alpha, y)$$

$$w(0, y) = w(L \sin \alpha, y)$$

$$P(0, y) = P(L \sin \alpha, y) - (\Delta P_{r+g})_z$$

$$\text{where } (\Delta P_{r+g})_z = \text{const}$$

All velocity derivatives must also be the same to satisfy the periodicity boundary conditions

$$\frac{\partial^{n+m} v(0, y)}{\partial y^n \partial z^m} = \frac{\partial^{n+m} v(L \sin \alpha, y)}{\partial y^n \partial z^m}$$

$$\frac{\partial^{n+m} w(0, y)}{\partial y^n \partial z^m} = \frac{\partial^{n+m} w(L \sin \alpha, y)}{\partial y^n \partial z^m}$$

for  $0 \leq n, m \leq \infty$

(4) Boundary condition for  $\partial P / \partial x$  for a cylindrical geometry (visco-seal).

In appendix B it is shown that for a cylindrical geometry  $\partial P / \partial x$  depends on the  $(\Delta P_{r+g})$  obtained in the z-direction

$$\frac{\partial P}{\partial x} = \frac{N(\Delta P_{r+g})_z}{2\pi R \cos \alpha}$$

These equations (9), (11), and (12) can be solved for the velocity components. The velocity components can be obtained for arbitrary  $(\Delta P_{r+g})_z$ . Then the axial pressure gradient  $\partial P / \partial L'$  can be found from

$$\frac{\partial P}{\partial L'} = \frac{\Delta P_{\text{axial}}}{L'} = \frac{(N)(\Delta P_{r+g})_z}{L} \cot \alpha$$

where  $L'$  is the axial length (see fig. 21). Qualitative pressure distribution from experimental data in the x- and z-directions is shown in figures 22 and 23.

By examining the analysis, boundary conditions, and the derived equations, the axial pressure gradient  $\partial P / \partial L'$  is a function of  $(\sigma, U, \rho, \nu)$ , where  $\sigma$  is a shape parameter that is a function of  $(b/h_o, c/h_o, a/b, \alpha)$ .

Since convective inertia effects are important, new geometric parameters appear which are not implied in creeping flow theory. Most notable of these is the aspect ratio  $b/h_0$ , which implies the degree of convective effect. When the  $b/h_0$  and  $a/b$  ratios are known,  $N$ , the number of helix or groove starts, can be found. (Direct effect of  $N$  is seen from boundary condition (4).) Thus the number of groove or helix starts also is an important parameter. Since inertia is important, a high density is desired for pressure generation.

The equations (9) to (12) and boundary conditions are the minimum number of terms that are necessary to mathematically describe the physics of the internal flow. This is the simplified form of the Navier Stokes equations which should be used for an analytical solution; however, a mathematical function to describe the groove-ridge shape may be too complex for a closed-form analytical solution. Thus the equations are solvable by using high speed digital computer numerical methods. Since numerical schemes can accommodate all two independent variable terms with equal ease, it is suggested that the complete set of two-dimensional equations be solved numerically, i. e.,

$$v \frac{\partial v}{\partial y} + w \frac{\partial v}{\partial z} = - \frac{1}{\rho} \frac{\partial P}{\partial y} + \nu \left( \frac{\partial^2 v}{\partial y^2} + \frac{\partial^2 v}{\partial z^2} \right) \quad (13)$$

$$v \frac{\partial w}{\partial y} + w \frac{\partial w}{\partial z} = - \frac{1}{\rho} \frac{\partial P}{\partial z} + \nu \left( \frac{\partial^2 w}{\partial y^2} + \frac{\partial^2 w}{\partial z^2} \right) \quad (11)$$

$$v \frac{\partial u}{\partial y} + w \frac{\partial u}{\partial z} = - \frac{1}{\rho} \frac{\partial P}{\partial x} + \nu \left( \frac{\partial^2 u}{\partial y^2} + \frac{\partial^2 u}{\partial z^2} \right) \quad \text{where } \frac{\partial P}{\partial x} = \text{constant} \quad (14)$$

$$\frac{\partial v}{\partial y} + \frac{\partial w}{\partial z} = 0 \quad (12)$$



Of course, the numerical solution will determine under what conditions the previously derived simplified form of the two dimensional Navier Stokes equations are good approximations.

By examining the set of equations (11) to (14) it is seen that  $v$  and  $w$  can be calculated from equations (11), (12), and (13). The solution is identical to a two-dimensional flow case. Then the  $u$  flow field can be found from equation (14) which is linear in  $u$ . This is an example of the Independence Principle.

From appendix A the energy equation with no temperature variation along the groove-ridge direction ( $\partial T / \partial x = 0$ ) is

$$v \frac{\partial \theta}{\partial y} + w \frac{\partial \theta}{\partial z} = \frac{\nu}{Pr} \left( \frac{\partial^2 \theta}{\partial y^2} + \frac{\partial^2 \theta}{\partial z^2} \right) + \frac{\mu}{\rho g C} \Phi + \frac{Q^*}{\rho g C} \quad (15)$$

Comparing the above equation with the  $x$ -direction momentum equation it is seen that the mathematical form of both equations is identical.

Substituting  $\theta \Rightarrow u$

and

$$\frac{\mu}{\rho g C} \Phi \quad \text{or} \quad \frac{Q^*}{\rho g C} = \text{a constant} \Rightarrow -\frac{1}{\rho} \frac{\partial P}{\partial x}$$

Thus with  $Pr = 1$  and the above substitutions, the equations (14) and (15) are identical. The thermal boundary conditions are

At  $y = 0$

$$\theta = \text{constant} \Rightarrow w = -U \sin \alpha = \text{constant}$$

At  $y = h(z)$

$$\theta = 0 \Rightarrow w = 0$$

and the boundary conditions are similar in form.

The above statements mean that once the  $u$  velocity field is found

the solution will also give the temperature distribution for the stated restrictions of constant frictional heating or a heat source in the fluid with the appropriate physical parameters equivalent to the constant pressure gradient along the groove-ridge pair direction and  $Pr = 1$ . Note that this temperature distribution solution violates the initial assumption of constant thermophysical properties; however, for small temperature differences the above solution will give a good qualitative picture of thermal effects.

## DISCUSSION

### Discussion of Equations

This analysis is valid only for a homogeneous fluid and figures 18 and 19 clarify the region of validity. The analysis is not valid for a scavenging area and a region consisting of a mixture of gas and liquid (see fig. 18) or under conditions of gas ingestion.

It should also be pointed out that the analysis is not valid in the end effect region at the high pressure end of the seal (see fig. 18) where the groove connects with the cavity. Since the appropriate equations are non-linear, the pressure is not a harmonic function; thus, the usual analog methods of finding end effect are not available as found in creeping flow regions (see appendix C).

The equations are unique in many ways. Mathematically, the problem has been reduced to two dimensions (y- and z-directions) but all three velocity components are present. Thus the flow field can be described as quasi-two-dimensional. Also, there is a pressure gradient in the third dimension (x-direction), but fortunately this gradient is a constant and dependent on the y- and z-direction gradients.

The velocity component  $v$  is no longer negligible as it was in the creeping flow solution. Physically,  $v$  cannot be negligible because of the presence of the edge effect which will result in a component of velocity in the  $y$ -direction.

Since there is no restriction on net volume flow, the pressure generation prediction equations should equally apply to hydrodynamic seals, bearings, and pumps.

When further examining the physics of the problem, it is seen that across the groove-ridge pairs the unbalance of the convective acceleration force with the drag force results in a pressure gradient in the  $z$ -direction. Since the step or edge causes the convective acceleration, its effects are not negligible unless there is a very large aspect ratio and the mathematical model accounts for the edge effect. Along the groove and ridge ( $x$ -direction) the drag force is in equilibrium with the induced pressure and convective inertia force. The drag force not only causes fluid motion but also aids in maintaining equilibrium with the pressure along the groove or ridge.

Both equations of motion illustrate the coupling of  $u$ ,  $v$ , and  $w$  in the convective inertia terms. This means that physically a condition such as no end leakage is possible. In creeping flow there is no coupling between the velocity components, which illustrates the shortcoming of that analysis (i. e., end leakage is not zero).

The assumption that the inertia terms are of the same order as the viscous terms results in equations of the boundary layer type; however, the boundary conditions are different.

The equations are of a form that might tempt one to reduce the number of independent variables by one by trying to find the admissible flow field which would result in a similarity transform solution. This technique fails because of the characteristic lengths that are present in this type of confined flow.

The equations are solvable by using high-speed digital computer numerical methods. A mathematical function to describe the groove-ridge shape may be too complex for a closed-form analytical solution. It should be interesting to find out if the step is still the optimum shape with convective inertia effects included. For creeping flow, Lord Rayleigh found in 1912 that the step was the optimum shape by using calculus of variations.

The equations and ordering procedure should be reexamined carefully before extending these results beyond the assumptions used in this analysis.

#### Discussion of Modified Reynolds Number

A check was made on the significance of the modified or reduced Reynolds number by calculating  $Re^*$  from the available published data at the claimed onset of turbulence (breakpoint). In table III it can be noted that the departure in all cases from a constant sealing coefficient occurred when  $Re^*$  was in the range of 0.26 to 2.2, which suggests that the so-called beginning of turbulent operation is really the beginning of significant convective inertia effects. This would be in agreement with Kettleborough (ref. 29), who found qualitative agreement between his inertia solution and experimental turbulent results.

For seals 5, 6, and 7 (see ref. 27 and table III), only the groove to ridge ratio has changed. As the ratio increases, the breakpoint decreases.

This is reasonable since a larger ridge area results in a less influential convective inertia effect and delays the beginning of pronounced convective inertia effects. It can also be seen in table III that the calculated  $Re^*$  are within an order of magnitude of one another for all of the experimenters. It is difficult, nevertheless, to select the breakpoint (see fig. 24). Even in a range of possible breakpoint numbers, however, the order of magnitude will remain the same. Further experimental results will be necessary, but in general, it can be concluded that if  $Re^* > 1$ , a constant sealing coefficient or bearing number will not exist.

In figure 25 it is seen that classically the empirical sealing parameter  $\lambda G$  was thought to be a constant until some critical  $Re_c$  and then to vary exponentially in the turbulent regime. The creeping flow solution was thought to be valid until the critical  $Re_c$  and then a semiempirical turbulent theory had to be used. Actually, the onset of significant convective inertia may be gradual, as shown in figure 25. Data (from ref. 27) for seal 7 in figure 24 tends to show this. The derived equations herein pertain to all cases under assumptions stated and will break down only under strong turbulence or an unknown instability phenomena. However, even in the turbulent flow model the convective inertia terms must be considered in addition to the Reynolds' stress terms. This is specifically shown by Kulinski and Ostrach (ref. 33) in their critical evaluation of high speed fluid film lubrication theory.

#### Principle of Viscoseal Operation

The classical explanation of viscoseal operation is now described. Since the seal is "pumping" the sealed fluid as fast it is leaking out, there is no net end flow (zero leakage). From the basic laws of fluid mechanics,

however, it is seen that the viscoseal axial pressure gradient results from the unbalance of the convective inertia force across the groove-ridge pairs and the drag force. The convective inertia force is much greater than the opposing drag force, and this results in a net pressure force. Along the groove-ridge direction, the drag force maintains equilibrium with the pressure force and convective inertia force. All three velocity components are "coupled," and thus zero net leakage is achieved. This is an excellent example of the physical importance of a nonlinear effect. The inadequacy of the linear theory (creeping flow) has been previously discussed.

## SUMMARY OF RESULTS

### Pressure Patterns

Pressure patterns were studied for a viscoseal in the laminar-flow regime with a mineral oil and the following results were obtained:

1. For the condition of helical grooves in direct connection with the pressurized cavity, the end effect is evidenced by a sharp decay of land leading-edge pressure.
2. No significant change in end-effect length was noted over the speed range investigated (modified Reynolds numbers ( $Re^*$ ) of 0.04 to 0.25).
3. Circumferential pressure gradients in the plane of rotation (plane orthogonal to  $\eta$ -axis) increase linearly across the groove and decrease linearly across the land. This pressure pattern repeats for each groove-land pair and provides a saw-tooth pressure profile around the circumference. The pressure gradients along the groove and land were linear.

### Gas Ingestion and Sealing Capacity

Visual observations and experimental evaluation of viscoseal assemblies with water (modified Reynolds numbers of 1.75 to 10.84) and sodium

(modified Reynolds numbers of 8.66 to 50.50) as sealed fluids disclosed the following:

1. Gas ingestion characteristics were fundamentally different for the helically grooved rotor-smooth bore housing combination. In the grooved housing-smooth rotor combination, centrifugal action tended to hold the gas bubbles out of the groove; thus the bubbles tended to escape over the lands rather than be pumped into the seal high-pressure end and a condition of no gas ingestion could be achieved. In the grooved rotor-smooth bore housing combination, centrifugal action forced the gas bubbles into the rotor grooves; thus the gas bubbles were pumped into the seal high-pressure end and increasing speeds resulted in increasing gas ingestion.

2. In sealing sodium, the grooved housing-smooth rotor combination had no detectable gas ingestion rate, but the grooved rotor-smooth bore housing combination showed increasing gas ingestion with increasing Reynolds number.

3. No gas ingestion occurred when sealing water with either the grooved rotor-smooth bore housing or the grooved housing-smooth rotor viscoseal when the liquid interface was stable (below Reynolds number ( $Re^*$ ) of 1.9).

4. In sealing sodium, the grooved housing-smooth rotor combination produced a higher sealing capacity (higher sealing parameter) than the grooved rotor-smooth bore housing combination. This was attributed to the presence of gas ingestion in the case of the grooved rotor.

5. Sealing, with negligible sodium leakage rate, was obtained for short operational periods (maximum length of continuous evaluation was

8 hr) over a pressure range of 20 to 100 lb force/sq in. gage and at sodium temperatures of 300° to 625° F.

### Theoretical Analysis of the Viscoseal

A review of the literature on the theoretical analysis of the viscoseal revealed that either the convective inertia forces or the viscous forces were neglected (inviscid fluid assumption). This analysis included both convective inertia and viscous forces. The following two-dimensional set of equations for a quasi-two-dimensional flow field were formulated and are solvable for the velocity and pressure distribution and optimum geometry utilizing numerical methods on a high-speed digital computer:

Conservation of momentum:

$$v \frac{\partial u}{\partial y} + w \frac{\partial u}{\partial z} = - \frac{1}{\rho} \frac{\partial P}{\partial z} + \nu \frac{\partial^2 u}{\partial y^2} \quad \text{where} \quad \frac{\partial P}{\partial x} = \text{constant} \quad (9)$$

$$\frac{\partial P}{\partial y} \cong 0 \quad (10)$$

$$v \frac{\partial w}{\partial y} + w \frac{\partial w}{\partial z} = - \frac{1}{\rho} \frac{\partial P}{\partial z} + \nu \left( \frac{\partial^2 w}{\partial y^2} + \frac{\partial^2 w}{\partial z^2} \right) \quad (11)$$

Conservation of mass:

$$\frac{\partial v}{\partial y} + \frac{\partial w}{\partial z} = 0 \quad (12)$$

With the following boundary conditions

(1) At the moving smooth plate surface,

$$u = U \cos \alpha \quad v = 0 \quad w = -v \sin \alpha$$

(2) At the fixed parallel groove geometry surface,

$$u = v = w = 0$$



## (3) Periodicity of groove-ridge pairs at the clearance interface.

For  $0 \leq y < h(z)$

$$v(0, y) = v(L \sin \alpha, y) \quad \text{and} \quad \frac{\partial^{n+m} v(0, y)}{\partial y^n \partial z^m} = \frac{\partial^{n+m} v(L \sin \alpha, y)}{\partial y^n \partial z^m}$$

$$w(0, y) = w(L \sin \alpha, y) \quad \text{and} \quad \frac{\partial^{n+m} w(0, y)}{\partial y^n \partial z^m} = \frac{\partial^{n+m} w(L \sin \alpha, y)}{\partial y^n \partial z^m}$$

$$P(0, y) = P(L \sin \alpha, y) - (\Delta P_{r+g})_z \quad \text{for} \quad 0 \leq n, m \leq \infty$$

(4)

$$\frac{\partial P}{\partial x} = \frac{N(\Delta P_{r+g})_z}{2\pi R \cos \alpha}$$

From the development and analysis of the equations, the following results and conclusions can be made:

1. A modified or reduced Reynolds number evolved which gives the relative magnitude of the convective inertia forces to the viscous forces:

$$Re^* \equiv Re_L \left( \frac{c}{L} \right)^2 \equiv Re_c \left( \frac{c}{L} \right) \quad \text{if} \quad \frac{c}{L} < 1$$

The characteristic length was selected to be the length of the groove-ridge pair in the direction of the smooth plate velocity vector. This is the principal length over which the driving force acts. The flow behavior over each groove-ridge pair is the same. Convective inertia effects can only be neglected if  $Re^* \ll 1$ , which will result in true creeping flow.

2. A modified Reynolds number equal to 1 will predict a significant change in sealing coefficient or bearing number which heretofore was attributed to the onset of turbulence. This means that the convective inertia effects are the foremost contributing factor to the improvement in sealing

coefficient or bearing number, not the turbulence effects. A calculation of the modified Reynolds number at the onset of turbulence of four different experimenters disclosed that the modified Reynolds number was near 1 ( $Re^* = 0.25$  to  $2.2$ ). Thus a turbulent flow analysis must also include the convective inertia terms in addition to the appropriate Reynolds stress terms.

3. Several additional parameters of pressure generation dependence were found that are not implied in the creeping flow analysis. These additional parameters, which arise from convective inertia effects, are the fluid density  $\rho$ , the groove width to depth or aspect ratio  $b/h_0$ , and the number of groove-ridge pairs  $N$ .

4. Solving equations (11) to (14) by numerical analysis will permit the investigation of arbitrary groove-ridge shape, for example, sinusoidal, rectangular, triangular, etc. Now a check can be made to see if a step is the optimum shape with convective inertia effects as it is for creeping flow.

5. The analysis provides a unified approach to parallel groove operation previously covered by creeping flow (sometimes called laminar flow) analysis and a semiempirical turbulent flow analysis.

6. No restriction was placed on the net flow situation between the plates. Therefore, the analysis can be used to analyze parallel groove geometries in hydrodynamic seals, bearings, and pumps.

7. The viscoseal axial pressure gradient results from the unbalance of the convective inertia force across the groove-ridge pairs and the drag force. Along the grooves or ridges, the drag force maintains equilibrium with the pressure force and the convective inertia force.

8. Zero leakage in viscoseal analysis can be attained through the consideration of convective acceleration terms (nonlinear effect). It is argued that the creeping flow analysis, which is a linear theory, cannot prove zero leakage.

9. The format of this analysis can be used to evaluate qualitative convective inertia effects in any step or converging wall hydrodynamic seal, pump, or bearing (Rayleigh step, journal bearing, etc.).

10. Solution of the  $u$  velocity (along the groove-ridge direction) will give an insight to the heat transfer in the viscoseal for the case when  $Pr = 1$ .

## APPENDIX A

### FORMAL ORDERING PROCEDURE FOR SIMPLIFYING BASIC EQUATIONS

The Navier-Stokes equations for a homogeneous incompressible Newtonian fluid, neglecting body forces and for steady flow, are

$$\rho \left( u \frac{\partial u}{\partial x} + v \frac{\partial u}{\partial y} + w \frac{\partial u}{\partial z} \right) = - \frac{\partial P}{\partial x} + \mu \left( \frac{\partial^2 u}{\partial x^2} + \frac{\partial^2 u}{\partial y^2} + \frac{\partial^2 u}{\partial z^2} \right) \quad (A1)$$

$$\rho \left( u \frac{\partial v}{\partial x} + v \frac{\partial v}{\partial y} + w \frac{\partial v}{\partial z} \right) = - \frac{\partial P}{\partial y} + \mu \left( \frac{\partial^2 v}{\partial x^2} + \frac{\partial^2 v}{\partial y^2} + \frac{\partial^2 v}{\partial z^2} \right) \quad (A2)$$

$$\rho \left( u \frac{\partial w}{\partial x} + v \frac{\partial w}{\partial y} + w \frac{\partial w}{\partial z} \right) = - \frac{\partial P}{\partial z} + \mu \left( \frac{\partial^2 w}{\partial x^2} + \frac{\partial^2 w}{\partial y^2} + \frac{\partial^2 w}{\partial z^2} \right) \quad (A3)$$

The incompressible continuity equation is

$$\frac{\partial u}{\partial x} + \frac{\partial v}{\partial y} + \frac{\partial w}{\partial z} = 0 \quad (A4)$$

To find the important terms in the previous flow field equations, a

formal ordering procedure will be used to determine the relative magnitudes of the terms.

The terms are normalized by scaling them to their appropriate maximum characteristic value as follows: let

$$\begin{aligned}\bar{x} &= \frac{x}{L \cos \alpha} & \bar{y} &= \frac{y}{c} & \bar{z} &= \frac{z}{L \sin \alpha} \\ \bar{u} &= \frac{u}{U \cos \alpha} & \bar{v} &= \frac{v}{V} & \bar{w} &= \frac{w}{U \sin \alpha}\end{aligned}$$

The characteristic dimensions  $c$  and  $L$  can be seen in figure 17. It is noted that a trigonometric relation exists between  $x$  and  $z$  characteristic lengths and that  $c/L < 1$ . The characteristic length was selected to be the length of the groove-ridge pair in the direction of the smooth plate velocity vector. This is the principal length over which the driving force acts. The flow behavior over each groove-ridge pair is the same.

Let  $\rho^*$  and  $\nu^*$  be the fluid density and viscosity corresponding to a reference state ( $P^*, T^*$ ). Therefore,

$$\bar{\nu} = \frac{\nu}{\nu^*} = 1$$

and

$$\bar{\rho} = \frac{\rho}{\rho^*} = 1$$

for incompressible fluids with constant thermophysical properties. Now to find the relative magnitude of  $V$  so that all terms of the incompressible continuity equation will be of the same order, the incompressible continuity equation is nondimensionalized:

$$\frac{\partial \bar{u}}{\partial \bar{x}} + \frac{V}{U} \frac{L}{c} \frac{\partial \bar{v}}{\partial \bar{y}} + \frac{\partial \bar{w}}{\partial \bar{z}} = 0 \quad (\text{A5})$$

To have all terms of the equation the same order of magnitude,  $\frac{V}{U} \frac{L}{c}$  must be of the order of 1. Therefore,  $V = U \frac{c}{L}$ , and thus  $\bar{v} = \frac{v}{U} \frac{L}{c}$ .

Next the equations of motion are nondimensionalized. The pressure term must first be nondimensionalized; even though the pressure is not the driving force, it is the function of primary importance. Thus the characteristic pressure is not extremely important. Since the pressure gradient is related to the rotor speed, it appears to be logical to nondimensionalize the pressure with respect to the dynamic pressure  $\rho U^2$  (also called the dynamic head):

$$\bar{P} = \frac{P}{\rho U^2}$$

It can be seen that the characteristic dynamic pressure  $\rho U^2$  has reduced the number of nondimensional groups by one (i. e., if  $P^*$  (a reference pressure) had been used, another nondimensional group would be present in the equations). Also, since the incompressible case is being analyzed, the pressure appears in the dynamic role only, not in the thermodynamic role.

#### Nondimensionalization of x-Direction Momentum Equation

When the x-direction momentum equation is nondimensionalized, equation (1) results in

$$u \frac{\partial \bar{u}}{\partial \bar{x}} + v \frac{\partial \bar{u}}{\partial \bar{y}} + w \frac{\partial \bar{u}}{\partial \bar{z}} = - \frac{1}{\cos^2 \alpha} \frac{\partial \bar{P}}{\partial \bar{x}} + \frac{\nu^*}{UL} \left[ \frac{1}{\cos^2 \alpha} \frac{\partial^2 \bar{u}}{\partial \bar{x}^2} + \left( \frac{L}{c} \right)^2 \frac{\partial^2 \bar{u}}{\partial \bar{y}^2} + \frac{1}{\sin^2 \alpha} \frac{\partial^2 \bar{u}}{\partial \bar{z}^2} \right]$$

Next a Reynolds number is defined based on the characteristic length  $L$ :

$$Re_L = \frac{UL}{\nu^*}$$

where

$$\nu = \nu^* \bar{\nu} = \nu^*$$

and thus

$$\begin{aligned} \bar{u} \frac{\partial \bar{u}}{\partial \bar{x}} + \bar{v} \frac{\partial \bar{u}}{\partial \bar{y}} + \bar{w} \frac{\partial \bar{u}}{\partial \bar{z}} = & - \frac{1}{\cos^2 \alpha} \frac{\partial \bar{P}}{\partial \bar{x}} \\ & + \frac{1}{Re_L} \left[ \frac{1}{\cos^2 \alpha} \frac{\partial^2 \bar{u}}{\partial \bar{x}^2} + \left( \frac{L}{c} \right)^2 \frac{\partial^2 \bar{u}}{\partial \bar{y}^2} + \frac{1}{\sin^2 \alpha} \frac{\partial^2 \bar{u}}{\partial \bar{z}^2} \right] \quad (A6) \end{aligned}$$

The convective acceleration and pressure terms are of unit order; thus, the viscous term must be of unit order also. The largest term of the viscous forces is  $\left( \frac{L}{c} \right)^2 \frac{\partial^2 \bar{u}}{\partial \bar{y}^2}$ , since  $\left( \frac{c}{L} \right) < 1$ ; therefore, the  $\frac{1}{Re_L} \left( \frac{L}{c} \right)^2$  should be of unit order. The modified Reynolds number is defined by  $Re^* = Re_L \left( \frac{c}{L} \right)^2$ . This is the identical "reduced" or "effective" Reynolds number that is used in the bearing theory to show the true relative magnitude of the inertia and viscous forces; therefore,

$$Re^* = \frac{\text{Inertia forces}}{\text{Viscous forces}}$$

(e. g., see ref. 32). Now for curved geometries, a Reynolds number based on clearance has appeared. This is especially true in viscoseal analysis where

$$Re_c = \frac{Uc}{\nu}$$

Writing the previous x-direction momentum equation in terms of  $Re_c$  gives

$$\bar{u} \frac{\partial \bar{u}}{\partial \bar{x}} + \bar{v} \frac{\partial \bar{u}}{\partial \bar{y}} + \bar{w} \frac{\partial \bar{u}}{\partial \bar{z}} = -\frac{1}{\cos^2 \alpha} \frac{\partial \bar{P}}{\partial \bar{x}} + \frac{\nu^*}{Uc} \left( \frac{c}{L} \frac{1}{\cos^2 \alpha} \frac{\partial^2 \bar{u}}{\partial \bar{x}^2} + \frac{L}{c} \frac{\partial^2 \bar{u}}{\partial \bar{x}^2} + \frac{c}{L} \frac{1}{\sin^2 \alpha} \frac{\partial^2 \bar{u}}{\partial \bar{z}^2} \right)$$

or

$$\bar{u} \frac{\partial \bar{u}}{\partial \bar{x}} + \bar{v} \frac{\partial \bar{u}}{\partial \bar{y}} + \bar{w} \frac{\partial \bar{u}}{\partial \bar{z}} = -\frac{1}{\cos^2 \alpha} \frac{\partial \bar{P}}{\partial \bar{x}} + \frac{1}{Re_c} \left( \frac{c}{L} \frac{1}{\cos^2 \alpha} \frac{\partial^2 \bar{u}}{\partial \bar{x}^2} + \frac{L}{c} \frac{\partial^2 \bar{u}}{\partial \bar{y}^2} + \frac{c}{L} \frac{1}{\sin^2 \alpha} \frac{\partial^2 \bar{u}}{\partial \bar{z}^2} \right)$$

Again it is seen that the  $\partial^2 \bar{u} / \partial \bar{y}^2$  term is the largest.

Thus  $1/Re_c(L/c)$  should be of unit order. Now

$$Re^* \equiv Re_c \left( \frac{c}{L} \right)$$

which leads to

$$Re^* \equiv Re_L \left( \frac{c}{L} \right)^2 \equiv Re_c \left( \frac{c}{L} \right)$$

It does not matter which Reynolds number is used to find the relative inertia force to viscous force ratio provided that  $c/L < 1$ , which corresponds to the conditions

$$\frac{\partial^2}{\partial y^2} \gg \frac{\partial^2}{\partial z^2}$$

and

$$\frac{\partial^2}{\partial y^2} \gg \frac{\partial^2}{\partial x^2}$$

The proper x-direction momentum equation then becomes

$$u \frac{\partial u}{\partial x} + v \frac{\partial u}{\partial y} + w \frac{\partial u}{\partial z} = -\frac{1}{\rho} \frac{\partial P}{\partial x} + \mu \frac{\partial^2 u}{\partial y^2} \quad (A7)$$

It is assumed that  $\alpha$  does not go to  $0^\circ$  or  $90^\circ$  for the formal ordering procedure to be valid.

### Example

A numerical example will be used to illustrate the validity of neglecting the  $\partial^2/\partial z^2$  and  $\partial^2/\partial x^2$  viscous terms. A typical viscoseal has the following construction and operating conditions: smooth 2-inch-diameter rotor, 0.0035-inch concentric radial clearance between the ridge (housing) and rotor surfaces, 1000 rpm, and sealed fluid (water) at  $60^\circ$  F. Therefore,

$$\nu = 17.5 \times 10^{-4} \text{ sq in. / sec}$$

$$c = 0.0035 \text{ in.}$$

$$U = 2\pi R(1000 \text{ rpm})/60 = 100 \text{ in. / sec (plate speed)}$$

$$c/R = 0.0035 \text{ (therefore, curvature effects should be slight)}$$

$$\begin{aligned} L &= \text{Ridge width} + \text{Groove width (in circumferential direction)} \\ &= 0.2 \text{ in.} + 0.2 \text{ in.} = 0.4 \text{ in.} \end{aligned}$$

$$\alpha = 15^\circ$$

$$\text{Re}_L = UL/\nu = 23,000$$

$$\text{Re}_c = Uc/\nu = 200$$

Using the Reynolds number based on the characteristic length  $L$  yields

$$\begin{aligned} \frac{1}{\text{Re}_L} \left[ \frac{1}{\cos^2 \alpha} \frac{\partial^2 \bar{u}}{\partial \bar{x}^2} + \left( \frac{L}{c} \right)^2 \frac{\partial^2 \bar{u}}{\partial \bar{y}^2} + \frac{1}{\sin^2 \alpha} \frac{\partial^2 \bar{u}}{\partial \bar{z}^2} \right] \\ = \frac{1}{\text{Re}_L} \left( 1.1 \frac{\partial^2 \bar{u}}{\partial \bar{x}^2} + 13,000 \frac{\partial^2 \bar{u}}{\partial \bar{y}^2} + 15 \frac{\partial^2 \bar{u}}{\partial \bar{z}^2} \right) \end{aligned}$$

Using the Reynolds number based on the clearance  $c$  gives



$$\begin{aligned} \frac{1}{\text{Re}_c} \left[ \left( \frac{c}{L} \right) \frac{1}{\cos^2 \alpha} \frac{\partial^2 \bar{u}}{\partial \bar{x}^2} + \left( \frac{L}{c} \right) \frac{\partial^2 \bar{u}}{\partial \bar{y}^2} + \left( \frac{c}{L} \right) \frac{1}{\sin^2 \alpha} \frac{\partial^2 \bar{u}}{\partial \bar{z}^2} \right] \\ = \frac{1}{\text{Re}_c} \left( 0.01 \frac{\partial^2 \bar{u}}{\partial \bar{x}^2} + 114 \frac{\partial^2 \bar{u}}{\partial \bar{y}^2} + 0.13 \frac{\partial^2 \bar{u}}{\partial \bar{z}^2} \right) \end{aligned}$$

In both equations it is seen that  $\partial^2 \bar{u} / \partial \bar{y}^2$  is the largest term. Now the modified or reduced Reynolds number is

$$\text{Re}^* = \text{Re}_L \left( \frac{c}{L} \right)^2 = \text{Re}_c \left( \frac{c}{L} \right) = 1.75$$

Nondimensionalization of y-Direction Momentum Equation

Nondimensionalizing the y-direction momentum equation (eq. (2))

yields

$$\bar{u} \frac{\partial \bar{v}}{\partial \bar{x}} + \bar{v} \frac{\partial \bar{v}}{\partial \bar{y}} + \bar{w} \frac{\partial \bar{v}}{\partial \bar{z}} = - \left( \frac{L}{c} \right)^2 \frac{\partial \bar{P}}{\partial \bar{y}} + \frac{1}{\text{Re}_L} \left[ \frac{1}{\cos^2 \alpha} \frac{\partial^2 \bar{v}}{\partial \bar{x}^2} + \left( \frac{L}{c} \right)^2 \frac{\partial^2 \bar{v}}{\partial \bar{y}^2} + \frac{1}{\sin^2 \alpha} \frac{\partial^2 \bar{v}}{\partial \bar{z}^2} \right] \quad (\text{A8})$$

Again using the definition of  $\text{Re}^*$  and examining the terms of unit order

$$\bar{u} \frac{\partial \bar{v}}{\partial \bar{x}}, \bar{v} \frac{\partial \bar{v}}{\partial \bar{y}}, \bar{w} \frac{\partial \bar{v}}{\partial \bar{z}}, \frac{1}{\text{Re}^*} \frac{\partial^2 \bar{v}}{\partial \bar{y}^2} \sim \mathcal{O}(1)$$

thus

$$\left( \frac{L}{c} \right)^2 \frac{\partial \bar{P}}{\partial \bar{y}} \cong \mathcal{O}(1)$$

Since

$$\frac{\partial \bar{P}}{\partial \bar{y}} \sim \mathcal{O} \left[ \left( \frac{c}{L} \right)^2 \right]$$

therefore

$$\frac{\partial P}{\partial y} \cong 0 \quad (A9)$$

This result is expected for a flat plate where there is no mechanism to generate a radial pressure gradient (e. g., a centrifugal force). For small curvatures,  $c/R \leq 0.1$  however, the radial pressure gradient  $\partial P/\partial y$  should also be a small quantity and have little physical influence on the axial pressure gradient. This can be shown by considering the following simplified model. Consider the flat plate model accelerating steadily about an origin. From elementary dynamics

$$\vec{a} = \hat{a}_t \hat{e}_t + a_n \hat{e}_n$$

where:  $a_t = \dot{q} = 0$  for steady acceleration

$$a_n = \frac{q^2}{R} = \frac{(u \cos \alpha - w \sin \alpha)^2}{R}$$

$q$  is the fluid velocity in the tangential plane (x-z plane) and

$q = u \cos \alpha - w \sin \alpha$  (see fig. 17).  $\hat{e}_n$  is the unit normal that is directed towards the axis of rotation. This is the y-coordinate direction in the flat plate model. Thus the centrifugal inertia force effects the y-momentum equation only.

Add  $\rho a_n$  to the inertia force in equation (A2) and nondimensionalize as before and let  $U = U\bar{U}$  and  $R = R\bar{R}$ . Thus equation (A8) becomes

$$\begin{aligned} \bar{u} \frac{\partial \bar{v}}{\partial \bar{x}} + \bar{v} \frac{\partial \bar{v}}{\partial \bar{y}} + \bar{w} \frac{\partial \bar{v}}{\partial \bar{z}} + \frac{1}{\bar{R}} \left( \frac{L}{c} \right)^2 \left( \frac{c}{R} \right) (-\sin \alpha \bar{w} + \cos \alpha \bar{u})^2 = - \left( \frac{L}{c} \right)^2 \frac{\partial \bar{P}}{\partial \bar{y}} \\ + \frac{1}{\text{Re}_L} \left[ \frac{1}{\cos^2 \alpha} \frac{\partial^2 \bar{v}}{\partial \bar{x}^2} + \left( \frac{L}{c} \right)^2 \frac{\partial^2 \bar{v}}{\partial \bar{y}^2} + \frac{1}{\sin^2 \alpha} \frac{\partial^2 \bar{v}}{\partial \bar{z}^2} \right] \quad (A8a) \end{aligned}$$

Now

$$\frac{1}{\bar{R}} \left( \frac{L}{c} \right)^2 \left( \frac{c}{R} \right) (-\sin \alpha \bar{w} + \cos \alpha \bar{u})^2 \sim \mathcal{O}(1)$$

Comparing the largest viscous term, pressure and centrifugal inertia term

$$\frac{\partial \bar{P}}{\partial \bar{y}} = \frac{1}{\text{Re}_L} \frac{\partial^2 \bar{v}}{\partial \bar{y}^2} + \frac{1}{\bar{R}} \left( \frac{c}{R} \right) (-\sin \alpha \bar{w} + \cos \alpha \bar{u})^2$$

Now use a typical  $\text{Re}_L$  (as in example)  $\cong 10^3$  and apply restriction

$$\frac{c}{R} < 0.01$$

$$\frac{\partial \bar{P}}{\partial \bar{y}} \cong (10^{-3}) \frac{\partial^2 \bar{v}}{\partial \bar{y}^2} + \frac{(10^{-2})}{\bar{R}} (-\sin \alpha \bar{w} + \cos \alpha \bar{u})^2$$

Again

$$\frac{\partial \bar{P}}{\partial y} \cong 0$$

if

$$\frac{c}{R} < 0.01$$

which substantiates the claim that the centrifugal effects should be small. In this model Coriolis forces were also thought to be negligible. The above centrifugal effect is for the case when the grooves are on the stationary housing. A slight modification is required for the groove-ridge pattern rotating. Note that as  $c/R \rightarrow 1$  the centrifugal force effects are no longer negligible.

#### Nondimensionalization of z-Direction Momentum Equation

In a like manner the z-direction momentum equation is nondimensionalized and appears in a similar form as the nondimensional x-direction momentum equation (A6)

$$\bar{u} \frac{\partial \bar{w}}{\partial \bar{x}} + \bar{v} \frac{\partial \bar{w}}{\partial \bar{y}} + \bar{w} \frac{\partial \bar{w}}{\partial \bar{z}} = -\frac{1}{\sin^2 \alpha} \frac{\partial \bar{P}}{\partial \bar{z}} + \frac{\nu^*}{UL} \left[ \frac{1}{\cos^2 \alpha} \frac{\partial^2 \bar{w}}{\partial \bar{x}^2} + \left(\frac{L}{c}\right)^2 \frac{\partial^2 \bar{w}}{\partial \bar{y}^2} + \frac{1}{\sin^2 \alpha} \frac{\partial^2 \bar{w}}{\partial \bar{z}^2} \right] \quad (\text{A10})$$

Examining the viscous terms

$$\frac{1}{\text{Re}_L} \left[ \frac{1}{\cos^2 \alpha} \frac{\partial^2 \bar{w}}{\partial \bar{x}^2} + \left(\frac{L}{c}\right)^2 \frac{\partial^2 \bar{w}}{\partial \bar{y}^2} + \frac{1}{\sin^2 \alpha} \frac{\partial^2 \bar{w}}{\partial \bar{z}^2} \right]$$

The largest term is  $(L/c)^2 (\partial^2 \bar{w} / \partial \bar{y}^2)$  and it would appear that the  $\partial^2 \bar{w} / \partial \bar{z}^2$  term could be neglected; however, this term must be retained due to a physical argument. Because of the "edge" there is a sharp gradient in the z-direction and the nature of the flow is such that the  $\partial^2 \bar{w} / \partial \bar{z}^2$  term must be retained. Thus the z-direction momentum equation in dimensional form is

$$u \frac{\partial w}{\partial x} + v \frac{\partial w}{\partial y} + w \frac{\partial w}{\partial z} = -\frac{1}{\rho} \frac{\partial P}{\partial z} + \nu \left( \frac{\partial^2 w}{\partial y^2} + \frac{\partial^2 w}{\partial z^2} \right) \quad (\text{A11})$$

This was pointed out by Dr. A. Mager of Aerospace Corporation, Los Angeles, California (personal communication, October 5, 1966).

#### Nondimensionalization of the Energy Equation

The energy equation for steady temperature variation for an incompressible fluid with constant thermophysical properties and negligible compression work is

$$u \frac{\partial T}{\partial x} + v \frac{\partial T}{\partial y} + w \frac{\partial T}{\partial z} = \frac{k}{\rho g C} \left( \frac{\partial^2 T}{\partial x^2} + \frac{\partial^2 T}{\partial y^2} + \frac{\partial^2 T}{\partial z^2} \right) + \frac{\mu}{\rho g C} \Phi + \frac{Q^*}{\rho g C} \quad (\text{A12})$$

Nondimensionalize as before and nondimensionalize the temperature by letting

$$\theta = \frac{T - T_s}{T_M - T_s} \quad \text{and} \quad \Phi' = \frac{\Phi}{\Phi^*}$$

Thus

$$\begin{aligned} \bar{u} \frac{\partial \theta}{\partial \bar{x}} + \bar{v} \frac{\partial \theta}{\partial \bar{y}} + \bar{w} \frac{\partial \theta}{\partial \bar{z}} = & \left( \frac{k}{\rho g C} \frac{L}{U c^2} \right) \left[ \left( \frac{c}{L} \right)^2 \frac{1}{\cos^2 \alpha} \frac{\partial^2 \theta}{\partial \bar{x}^2} + \frac{\partial^2 \theta}{\partial \bar{y}^2} + \left( \frac{c}{L} \right)^2 \frac{1}{\sin^2 \alpha} \frac{\partial^2 \theta}{\partial \bar{z}^2} \right] \\ & + \frac{\Phi'}{L \rho g C (T_M - T_S)} + \frac{Q^*}{\rho g C (T_M - T_S)} \end{aligned}$$

now

$$\left( \frac{k}{\rho g C} \frac{\nu}{U c} \frac{L}{c} \right) = \frac{1}{Pr} \frac{1}{Re_c} \left( \frac{L}{c} \right) = \frac{1}{Pr Re^*} = \frac{1}{P_e^*}$$

where  $P_e^*$  is the modified Péclet number

$$P_e^* = P_e \left( \frac{c}{L} \right) = Pr Re_c \left( \frac{c}{L} \right)$$

or

$$\begin{aligned} \bar{u} \frac{\partial \theta}{\partial \bar{x}} + \bar{v} \frac{\partial \theta}{\partial \bar{y}} + \bar{w} \frac{\partial \theta}{\partial \bar{z}} = & \frac{1}{P_e^*} \left[ \left( \frac{c}{L} \right)^2 \frac{1}{\cos^2 \alpha} \frac{\partial^2 \theta}{\partial \bar{x}^2} + \frac{\partial^2 \theta}{\partial \bar{y}^2} + \left( \frac{c}{L} \right)^2 \frac{1}{\sin^2 \alpha} \frac{\partial^2 \theta}{\partial \bar{z}^2} \right] \\ & + \frac{\Phi'}{L \rho g C (T_M - T_S)} + \frac{Q^*}{\rho g C (T_M - T_S)} \end{aligned}$$

Now assume constant temperature in the x-direction (along the groove ridge pairs) then

$$\bar{v} \frac{\partial \theta}{\partial \bar{y}} + \bar{w} \frac{\partial \theta}{\partial \bar{z}} = \frac{1}{P_e^*} \left[ \frac{\partial^2 \theta}{\partial \bar{y}^2} + \frac{1}{\sin^2 \alpha} \left( \frac{c}{L} \right)^2 \frac{\partial^2 \theta}{\partial \bar{z}^2} \right] + \frac{\Phi'}{L \rho g C (T_M - T_S)} + \frac{Q^*}{\rho g C (T_M - T_S)}$$

Now dimensionalize all terms but the temperature

$$v \frac{\partial \theta}{\partial y} + w \frac{\partial \theta}{\partial z} = \frac{k}{\rho g C} \left( \frac{\partial^2 \theta}{\partial y^2} + \frac{\partial^2 \theta}{\partial z^2} \right) + \frac{\mu}{\rho g C} \Phi + \frac{Q^*}{\rho g C}$$

$$\text{Pr} = \frac{C\mu}{k}$$

therefore

$$v \frac{\partial \theta}{\partial y} + w \frac{\partial \theta}{\partial z} = \frac{\nu}{\text{Pr}} \left( \frac{\partial^2 \theta}{\partial y^2} + \frac{\partial^2 \theta}{\partial z^2} \right) + \frac{\mu}{\rho g C} \Phi + \frac{Q^*}{\rho g C} \quad (\text{A13})$$

## APPENDIX B

### FORMULATION OF ALONG GROOVE-RIDGE BOUNDARY CONDITION FOR A CYLINDRICAL GEOMETRY (VISCOSEAL)

A special case of parallel groove geometry is a cylindrical geometry which is the helically grooved fluid film seal (viscoseal). For this cylindrical geometry a special boundary condition must be placed on the pressure gradient along the groove-ridge direction. This can best be illustrated by referring to figure 26. It is seen that the point o to point a can be traversed along both coordinate axes on the surface (x and z axes).

From figure 26 and figure 21, it is seen that going from point o to point a along the z-axis involves the traversing of an angle  $\varphi$ .

$$\tan \alpha = \frac{R\varphi}{L'} \quad (\text{B1})$$

Now going the same distance along the x-axis

$$\cot \alpha = \frac{2\pi R - R\varphi}{L'} \quad (\text{B2})$$

Equating (B1) and (B2)

$$\frac{2\pi - \varphi}{\tan \alpha} = \frac{\varphi}{\cot \alpha}$$

or

$$\varphi = 2\pi \cos^2 \alpha \quad (\text{B3})$$

The arc distance (path length) in the x-direction is:

$$S = \sqrt{(R\phi)^2 + (L')^2}$$

Upon substitution for  $L'$  and  $\phi$

$$S = 2\pi R \cos \alpha \quad (\text{B4})$$

The pressure differential at  $a$  from traversing the z-direction from  $o$  is

$$(\Delta P_{o-a} = (\Delta P_{r+g})_z (N)$$

then

$$\frac{\partial P}{\partial x} = \frac{N(\Delta P_{r+g})_z}{S} = \frac{N(\Delta P_{r+g})_z}{2\pi R \cos \alpha} \quad (\text{B5})$$

It is seen that  $\partial P / \partial x = \text{constant}$  which follows from fully developed flow along the groove-ridge direction and verified by experiment in reference 5.

## APPENDIX C

### SUMMARY OF CREEPING FLOW ANALYSIS

The optimization from creeping flow analysis has been formulated by considering a flat-plate model (unwrapped cylinders, see fig. 27) and the following:

(1) General incompressible plane Couette flow is assumed in the  $\xi$ -direction (Poiseuille flow and simple Couette flow). The  $\xi$ -direction momentum equation is

$$\frac{\partial^2 u_\epsilon}{\partial \zeta^2} = \frac{1}{\mu} \frac{\partial P}{\partial \xi}$$

with the boundary conditions

$$u_{\epsilon} = U \quad \text{at} \quad \zeta = 0$$

$$u_{\epsilon} = 0 \quad \text{at} \quad \zeta = h$$

where

$$h = c \quad \text{at ridge surface}$$

$$h = c + h_0 \quad \text{at groove root surface}$$

The well known solution (e.g., see ref. 32) is

$$u_{\epsilon} = \frac{\zeta}{h} U - \frac{h}{2\mu} \frac{dP}{d\xi} \zeta \left(1 - \frac{\zeta}{h}\right)$$

(2) Poiseuille flow is assumed in the  $\eta$ -direction. The  $\eta$ -direction momentum equation is

$$\frac{\partial^2 w_{\eta}}{\partial \zeta^2} = \frac{1}{\mu} \frac{\partial P}{\partial \eta}$$

with the boundary conditions

$$w_{\eta} = 0 \quad \text{at} \quad \zeta = 0$$

$$w_{\eta} = 0 \quad \text{at} \quad \zeta = h$$

The well-known solution (see ref. 32) is

$$w_{\eta} = \frac{1}{2\mu} \left( \frac{\partial P}{\partial \eta} \right) \zeta (\zeta - h)$$

Now the condition  $Q = 0$  is imposed in the control volume; that is,

$$Q = Q_{\xi} + Q_{\eta} = \iint u_{\epsilon} \, d\eta \, d\zeta + \iint w_{\eta} \, d\zeta \, d\xi = 0$$

which means that there is no net end leakage or closed channel flow. This is a restriction that limits the optimization and pressure gradient prediction to a seal only.

Solving for pressure gradient that satisfies the Reynolds equation (ref. 34) results in a sealing parameter



$$\frac{\Delta P}{L'} = \frac{6\mu UG}{c^2}$$

or

$$G = \frac{c^2}{6\mu U} \left( \frac{\Delta P}{L'} \right) = \frac{1}{\Lambda}$$

where  $\Lambda$  is the bearing number (ref. 34) and  $G$  is a geometry factor.

See references 1 to 26 for various expressions and values for  $G$ .

The creeping flow analysis has some paradoxes. It can best be illustrated by referring to figures 17 and 28 and by observing the resolution of the drag force into components along the groove (x-direction) and normal to the groove (z-direction). In creeping flow, the drag force is in equilibrium with the pressure force. Thus along the groove (x-direction) the drag force is indeed in equilibrium with the pressure force. In the normal groove direction (z-direction), however, the pressure and drag forces are in the same direction, which is also the direction of a very large pressure gradient (see figs. 22 and 23). Therefore, an unbalance of forces exists in this direction. Physically, the  $Q = 0$  restriction is not possible. Also, this point can be illustrated from  $\xi$ - and  $\eta$ -direction momentum equations, respectively:

$$\frac{\partial^2 u_\epsilon}{\partial \xi^2} = \frac{1}{\mu} \frac{\partial P}{\partial \xi}$$

$$\frac{\partial^2 w_\eta}{\partial \xi^2} = \frac{1}{\mu} \frac{\partial P}{\partial \eta}$$

Notice that there is no velocity "coupling" between the velocity components; that is,  $u_\epsilon$  and  $w_\eta$  are independent of one another. It is obvious that for zero leakage these velocity components are not independent of one

another. Thus, physically as well as mathematically it is not possible under the restrictions of the classical creeping flow analysis to get zero leakage.

Also in the creeping flow analysis the edge effects are assumed negligible. The full meaning of this assumption has not really been clarified; it is only close to physical reality when  $c$  is very small and/or  $b/h_0$  is very large. For example, the creeping flow analysis is valid for spiral groove thrust bearings where  $c$  is on the order of 500 microinches and the aspect ratio is on the order of 1000 ( $c/L \ll 1$ , see fig. 29). As  $b \rightarrow h_0$ , the edge effect becomes more pronounced as the convective forces becomes more and more important. To date only reference 35 has explicitly stated this restriction.

To resolve the paradox of having the drag and pressure forces unbalanced in the  $z$ -direction, a convective inertia force is in equilibrium with the pressure and drag forces (a nonlinear effect). The step is causing a convective change that results in generation of an axial pressure gradient. The role of the step is now described.

If a concentric rotor is rotating about a stationary smooth sleeve, no axial pressure gradient is generated. This is the classic axisymmetric Couette flow (see ref. 36). Furthermore, if an axial pressure gradient is imposed (e.g., by having the rotor translate in the axial direction) an "uncoupled" helical flow will result. Subsequently, of course, there will be net flow out.

In the helical groove seal (viscoseal), the step or edge  $h_0$  is the pressure generation mechanism. Without the step, that is, the limiting case when  $h_0 \rightarrow 0$  (rotor and housing smooth), there is no axial pressure

gradient generated. Eccentricity will generate a radial pressure gradient. Therefore, the effect of the groove wall is a convective acceleration or inertia effect (nonlinear effect). To neglect the convective force terms means that the primary axial pressure generating mechanism is neglected.

The creeping flow solution equations are linear and pressure is a potential function. The creeping motion or slow viscous flow momentum equation in vector notation is

$$\nabla P = \mu \nabla^2 \vec{V}$$

The incompressible continuity equation says

$$\nabla \cdot \vec{V} = 0$$

Taking the divergence of both sides of the equation yields

$$\nabla \cdot \nabla P = \mu \nabla^2 (\nabla \cdot \vec{V}) = 0$$

or

$$\nabla^2 P = 0$$

which is Laplace's equation, since pressure is a scalar quantity. Consequently, the multitude of mathematical analog methods of solving linear equations and specifically Laplace's equation can be used. Thus, solutions for end effect can readily be found (refs. 1 and 34).

Muijderman (ref. 1) used conformal mapping to analyze the spiral grooved bearing. Again, this technique can be readily applied because pressure is a potential function.

#### REFERENCES

1. Muijderman, E. A.: Spiral Groove Bearings. Philips Res. Rept. Suppl. 1964, no. 2.: See also Scientific Lubr., vol. 17, no. 1, Jan. 1965, pp. 12-17.

2. Rowell, H. S.; and Finlayson, D.: Screw Viscosity Pumps. Engineering, vol. 114, Nov. 1922, pp. 606-607.
3. Boon, E. F.; and Tal, S. E.: Hydrodynamic Seal for Rotating Shafts. DEG. Inf. Ser. 13, United Kingdom Atomic Energy Authority, 1961.
4. King, Alan E.: Screw Type Shaft Seals for Potassium Lubricated Generators. IEEE Trans. on Aerospace, vol. AS-3, Supplement, June 1965, pp. 471-479.
5. Ludwig, Lawrence P.; Strom, Thomas N.; and Allen, Gordon P.: Gas Ingestion and Sealing Capacity of Helical Groove Fluid Film Seal (Viscoseal) Using Sodium and Water as Sealed Fluids. NASA TN D-3348, 1966.
6. Ludwig, Lawrence P.; Strom, Thomas N.; and Allen, Gordon P.: Experimental Study of End Effect and Pressure Patterns in Helical Groove Fluid Film Seal (Viscoseal). NASA TN D-3096, 1965.
7. Vohr, J. H.; and Chow, C. Y.: Characteristics of Herringbone-Grooved Gas-Lubricated Journal Bearings. J. Basic Eng., vol. 87, no. 3, Sept. 1965, pp. 568-578.
8. Billet, A. B.: Hydraulic Sealing in Space Environments. Proceedings of the Second International Conference on Fluid Sealing, B. S. Nau, H. S. Stephens, and D. E. Turnbull, eds., British Hydromechanics Research Association, Harlow, Essex, England, 1964, pp. C2-17 - C2-36.
9. Rowell, H. S.; and Finlayson, D.: Screw Viscosity Pumps. Engineering, vol. 126, Aug. 1928, pp. 249-250.

10. Rowell, H. S.; and Finlayson, D.: Screw Viscosity Pumps. Engineering, vol. 126, Sept. 1928, pp. 385-387.
11. Rogowsky, Z.: Mechanical Principles of the Screw Extrusion Machine. Engineering, vol. 162, no. 4213, Oct. 11, 1946, pp. 358-360.
12. Strub, R. A.: Spindle Drag Pump. Machine Design, vol. 25, July 1953, pp. 149-151.
13. Pigott, W. T.: Pressures Developed by Viscous Materials in the Screw Extrusion Machine. ASME Trans., vol. 73, Oct. 1951, pp. 947-955.
14. Anon.: Theory of Extrusion. Ind. Eng. Chem., vol. 45, no. 5, May 1953, pp. 969-993.
15. Eccher, Silvio; and Valentinotti, Aldo: Experimental Determination of Velocity Profiles in an Extruder Screw. Ind. Eng. Chem., vol. 50, no. 5, May 1958, pp. 829-836.
16. Griffith, R. M.: Fully Developed Flow in Screw Extruders. Ind. Eng. Chem. Fundamentals, vol. 1, no. 3, Aug. 1962, pp. 180-187.
17. Squires, P. H.: Screw Extrusion - Flow Patterns and Recent Theoretical Developments. SPE Trans., vol. 4, no. 1, Jan. 1964, pp. 7-16.
18. McGrew, J. M.; and McHugh, J. D.: Analysis and Test of the Screw Seal in Laminar and Turbulent Operation. J. Basic Eng., vol. 87, no. 1, Mar. 1965, pp. 153-162.
19. Zotov, V. A.: Research on Helical Groove Seals. Russ. Eng. J., vol. 10, Oct. 1959, pp. 3-7.

20. Asanuma, T.: Studies on the Sealing Action of Viscous Fluids.  
Paper No. A3 presented at the First International Conference on Fluid Sealing. Cranfield, England. British Hydromechanics Research Association, Harlow, Essex, England, Apr. 1961.
21. Lessley, R. L.; and Hodgson, J. N.: Low-Leakage Dynamic Seal-to-Space. Paper 65-GTP-14, ASME, Feb. 1965.
22. Whipple, R. T. P.: The Inclined Groove Bearing. Rep. AERE-T/R-622 (rev.), Research Group, Atomic Energy Research Establishment, United Kingdom Atomic Energy Authority, 1958.
23. Gruntz, Robert D.; and Rackley, Ray A.: Snap 50/Spur Power Conversion System-Objectives, Current Status and Lunar Applications. Paper No. 650321, SAE, May 1965.
24. Golubiev, A. I.: Studies on Seals for Rotating Shafts of High-Pressure Pumps. Wear, vol. 8, no. 4, July/Aug. 1965, pp. 270-288.
25. Holan, Karel: Sealing in Engineering. Proceedings of the Second International Conference on Fluid Sealings, B. S. Nau, H. S. Stephens, and D. E. Turnbull, eds., British Hydromechanics Research Association, Harlow, Essex, England, 1964, pp. E5-73 - E5-88.
26. Stair, William K.: Analysis of the Visco Seal. Rep. No. ME 65-587-2, University of Tennessee, Jan. 18, 1965.
27. Stair, William K.: Theoretical and Experimental Studies of Visco-Type Shaft Seals. Rep. No. ME 66-587-5, University of Tennessee, Apr. 28, 1966.

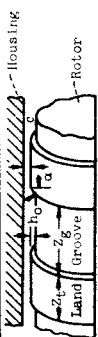
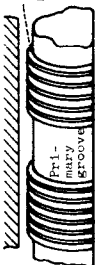
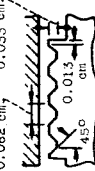
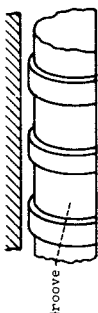
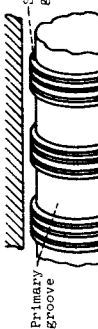
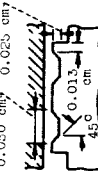
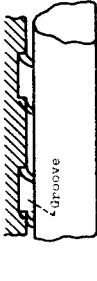
28. Lessley, R. L.: Snap-8 Seals-to-Space Development Test Program. Vol. 1 - Visco Pump. Rep. No. 2808 (Topical) (NASA CR-54234), Aerojet-General Corp., May 1964.
29. Kettleborough, C. F.: Turbulent and Inertia Flow in Slider Bearings, ASLE Trans., vol. 8, no. 3, July 1965, pp. 286-295.
30. Zuk, John; Ludwig, Lawrence P.; and Johnson, Robert L.: Flow and Pressure Field Analysis of Parallel Groove Geometry for an Incompressible Fluid With Convective Inertia Effects. NASA TN D-3635, 1966.
31. Kuivinen, David E.: Determination of Oxygen in Liquid Alkali Metals by the Mercury Amalgamation Method. Paper presented at the Nineteenth Meeting, Chemical Rocket Propulsion Group (St. Paul, Minn.), July-Aug., 1963.
32. Schlichting, Hermann (J. Kestin, Trans.): Boundary Layer Theory. Fourth ed., McGraw-Hill Book Co., Inc., 1960.
33. Kulinski, E. S.; and Ostrach, S.: A Critical Evaluation of the Status and Trends in High Speed Fluid Film Lubrication (to be published).
34. Bisson, Edmond E.; and Anderson, William J.: Advanced Bearing Technology. NASA SP-38, 1964.
35. Booy, M. L.: Influence of Oblique Channel Ends on Screw-Pump Performance. J. Basic Eng., vol. 88, no. 1, Mar. 1966, pp. 121-131.
36. Langlois, W. E.: Slow Viscous Flow. Macmillan Co., 1964, pp. 105-107.

**TABLE I. - VISCOSITY  
OF MINERAL OIL**

Temperature		Kinematic viscosity, cs
<sup>o</sup> F	<sup>o</sup> C	
100	37.8	71.2
130	54.4	32.4
210	98.9	8.4



TABLE II. - VISCOSEAL GEOMETRIES

Geometry	Configuration	Primary grooves					Secondary grooves				
		Groove width, $z_g$ , cm	Land width, $z_t$ , cm	Ratio of groove to land width, $z_g/z_t$	Groove depth, $h_o$	Radial clearance, c, cm	Primary helix angle, deg	Number of helix starts	Number of helix starts per land	Secondary helix angle, $\alpha_s$ , deg	Cross section through land
$a_1$		0.480 (0.190 in.)	0.33 (0.130 in.)	1.5	0.032 (0.013 in.)	0.010 (0.004 in.)	14.5	5	0	----	
2 (Geometry 1 plus secondary grooves)		0.480 (0.190 in.)	0.33 (0.130 in.)	1.5	0.032 (0.013 in.)	0.010 (0.004 in.)	14.5	5	4	14.5	
3		0.266 (0.105 in.)	0.14 (0.055 in.)	1.9	0.032 (0.013 in.)	0.010 (0.004 in.)	14.5	10	0	----	
4 (Geometry 3 plus secondary grooves)		0.266 (0.105 in.)	0.0140 (0.055 in.)	1.9	0.032 (0.013 in.)	0.010 (0.004 in.)	14.5	10	2	14.5	
5		0.480 (0.190 in.)	0.033 (0.130 in.)	1.5	0.032 (0.013 in.)	0.010 (0.004 in.)	14.5	5	0	----	

a<sub>1</sub> used as base line.

TABLE III. - CRITICAL MODIFIED REYNOLDS NUMBER FOR ONSET OF TURBULENCE OF VARIOUS EXPERIMENTERS

Experimenter	Reference and fluid	Seal	Diameter, in.	Radial clearance, c, in.	Ratio of radial clearance to rotor radius, c/R	Ridge width, a, in.	Groove width, b, in.	Helix angle, $\alpha$ , deg	Characteristic length, L, in.	Clearance Reynolds number, $Re_c$	Modified Reynolds number, $Re^*$
Stair	27 Water	a1	1.2430	0.0042	0.0068	0.0934	0.1596	14.5	1.01	400	1.7
		2	1.2465	.00235	.0038	.1176	.0494	9.67	.98	(b)	(b)
		2B	1.2420	.0047	.0076	.1176	.0494	9.67	.98	(b)	(b)
		3	1.2461	.00265	.0043	.0828	.0842	9.67	.98	350	.95
		3B	1.2408	.0053	.0085	.0828	.0842	9.67	.98	(b)	(b)
		4	1.2461	.00265	.0043	.0514	.1156	9.67	.98	200	.95
		4B	1.2408	.0053	.0085	.0514	.1156	9.67	.98	400	2.2
		5	1.2455	.00295	.0047	.1585	.0607	5.81	1.83	600	.97
		6	1.2455	.00295	.0047	.1070	.1083	5.81	1.83	200	.32
		7	1.2455	.00295	.0047	.0609	.1600	5.81	1.83	160	.26
King	4 and 27 Oil, water, potassium <sup>d</sup>	3C	2	0.0029	0.0029	0.1063	0.1063	3.86	3.2	550	0.50
		1B	2	.0020	.0020	.1063	.1063	3.86	3.2	400	.25
		2E	2	.0025	.0020	.1000	.1000	7.26	1.54	650	1.1
		5D	2	.0015	.0015	.1000	.1000	7.26	1.54	650	.63
McGrew and McHugh	18 Oil	SF96-5 oil	1	0.00325	0.0065	(c)	(c)	14.5	3.14	400	0.41
Lessley	28 Oil	Configura-tion B	2	0.0032	0.0032	0.075	0.122	14.5	0.79	350	1.4
	Water Mercury <sup>d</sup>	Configura-tion C	2	.0032	.0032	.083	.136	4	3.13	500	.51

<sup>a</sup>Eccentricity of rotor to housing,  $\epsilon = 0.1$ .<sup>b</sup>Break point not well defined.<sup>c</sup>Four thread starts.<sup>d</sup>Not explicitly found at breakpoint but falls on data line.

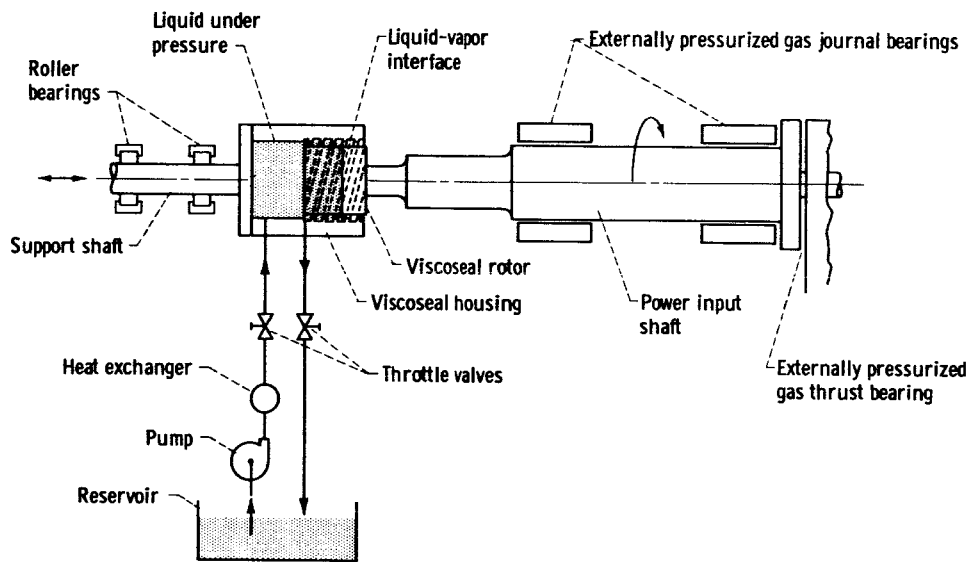


Figure 1. - Viscoseal and hydraulic system.

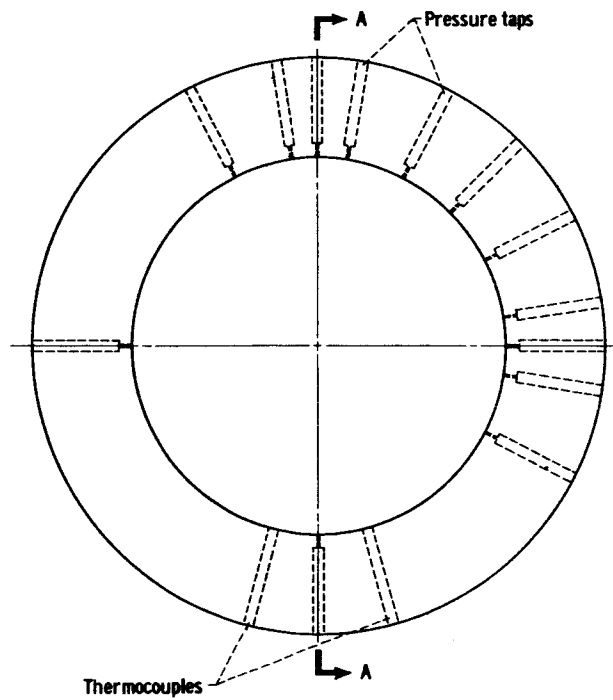
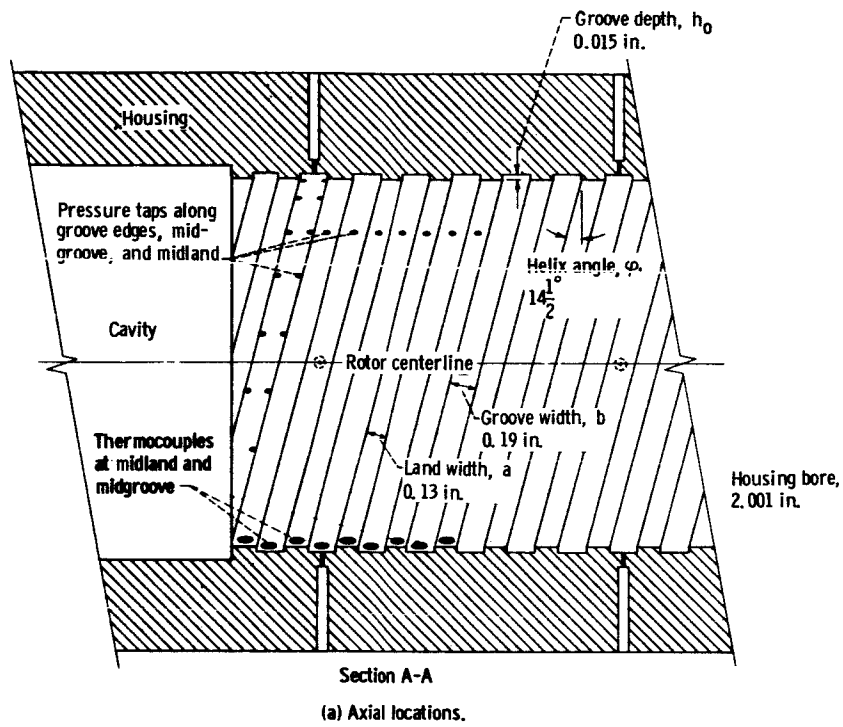


Figure 2 - Pressure tap and thermocouple locations.

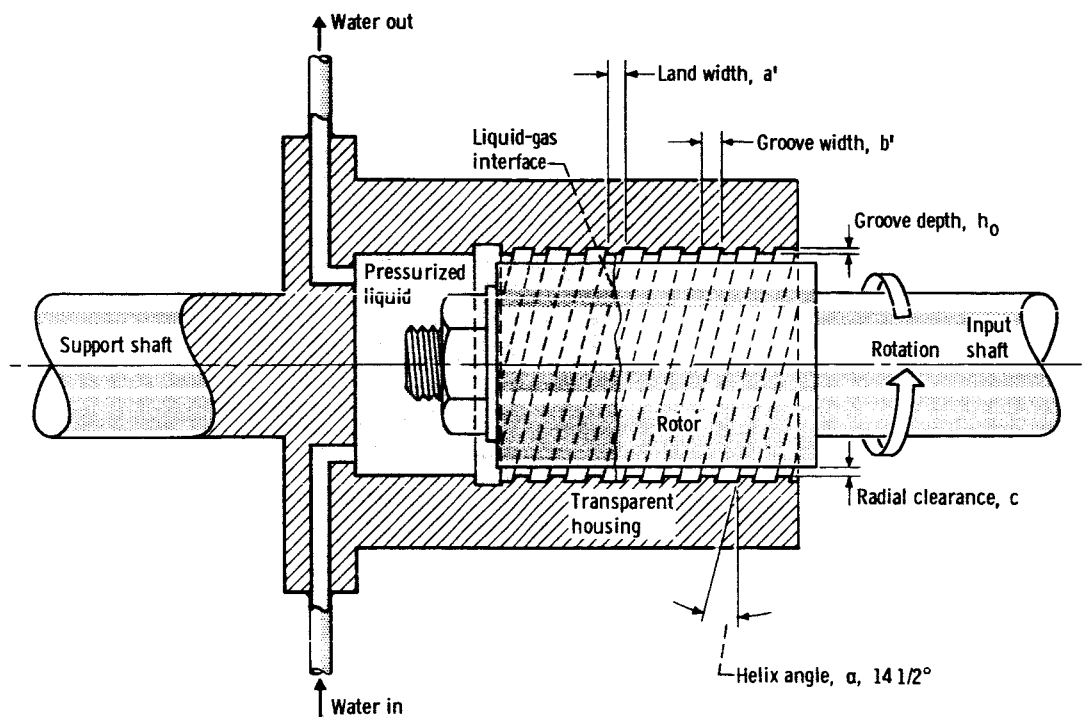


Figure 3. - Internal grooved housing viscoseal used with water.

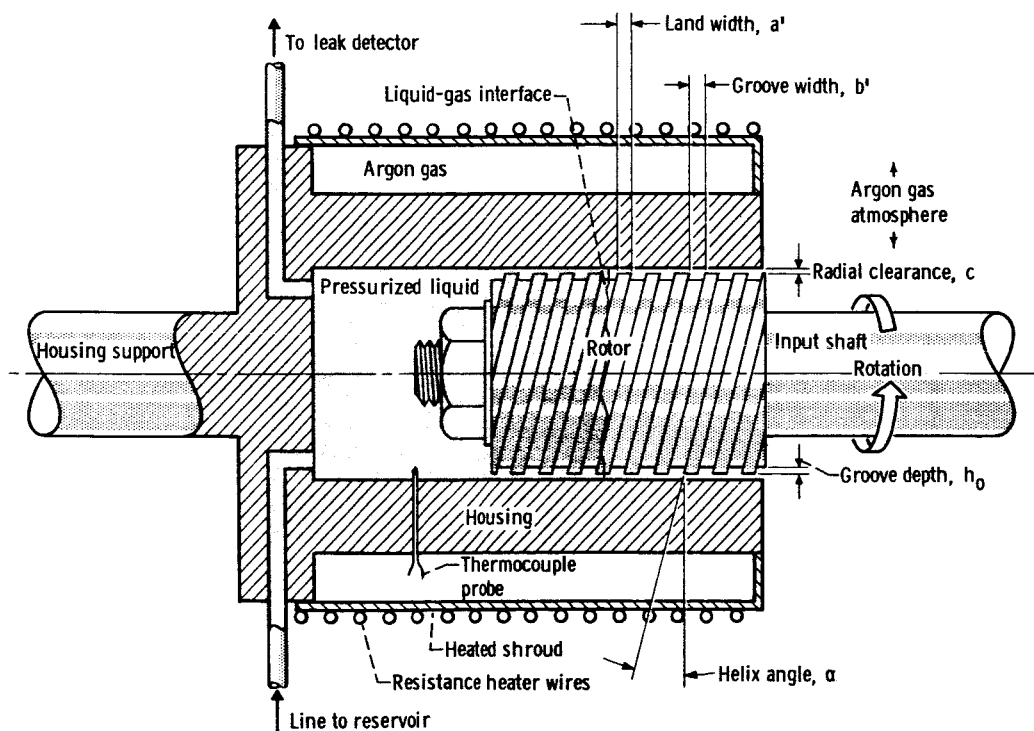


Figure 4. - Grooved rotor viscoseal used to seal sodium.

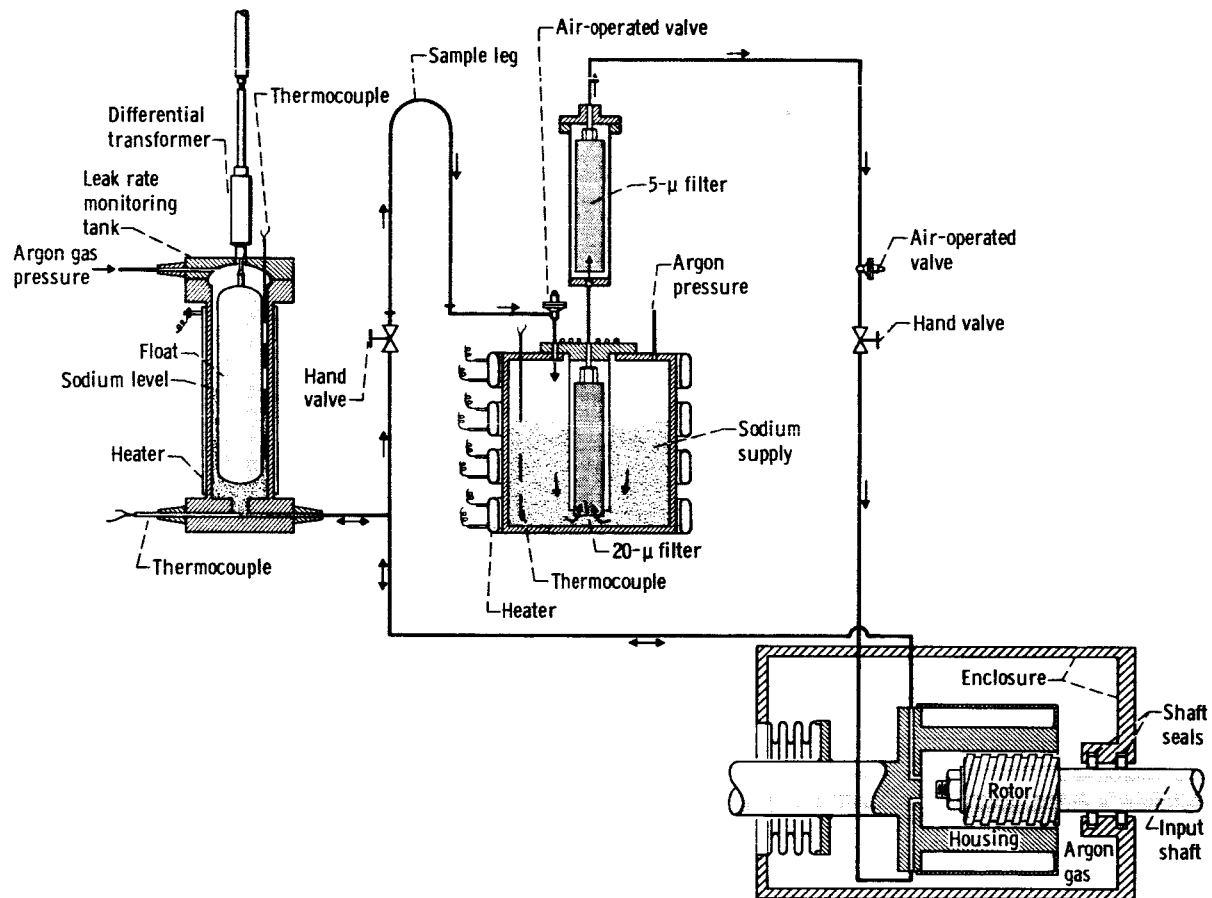


Figure 5. - Sodium supply system.

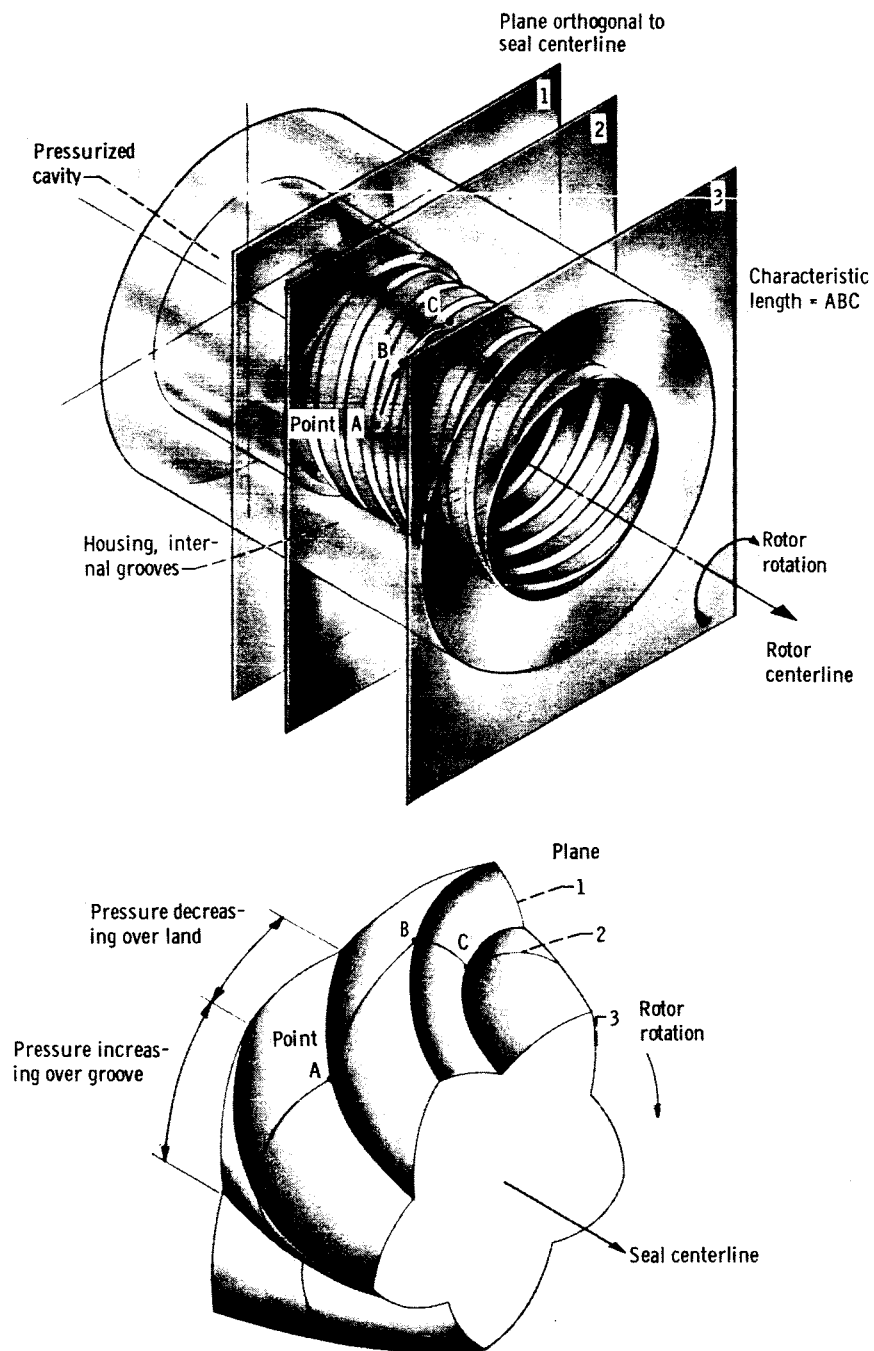


Figure 6. - Isometric representation of viscoseal and pressure patterns.

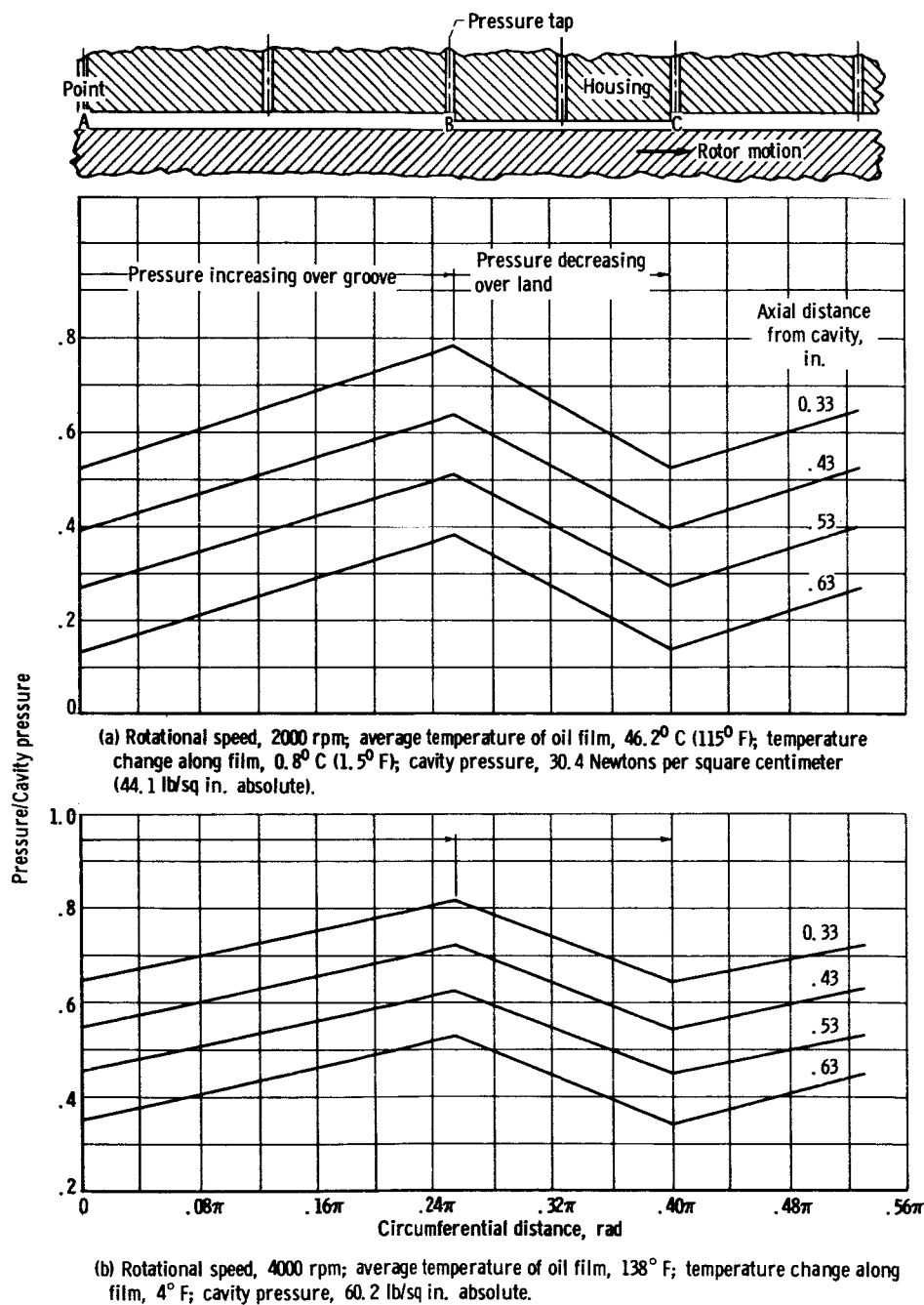
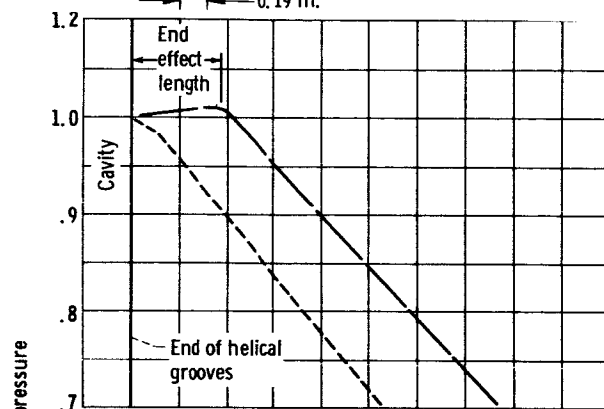
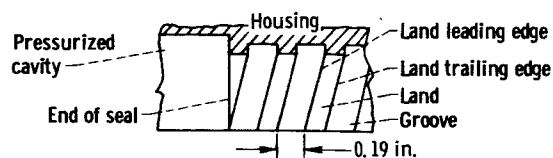
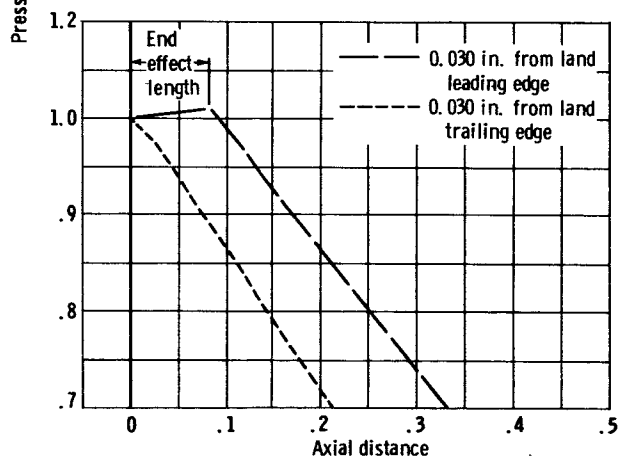


Figure 7. - Pressure gradients on planes orthogonal to viscoseal axis centerline.



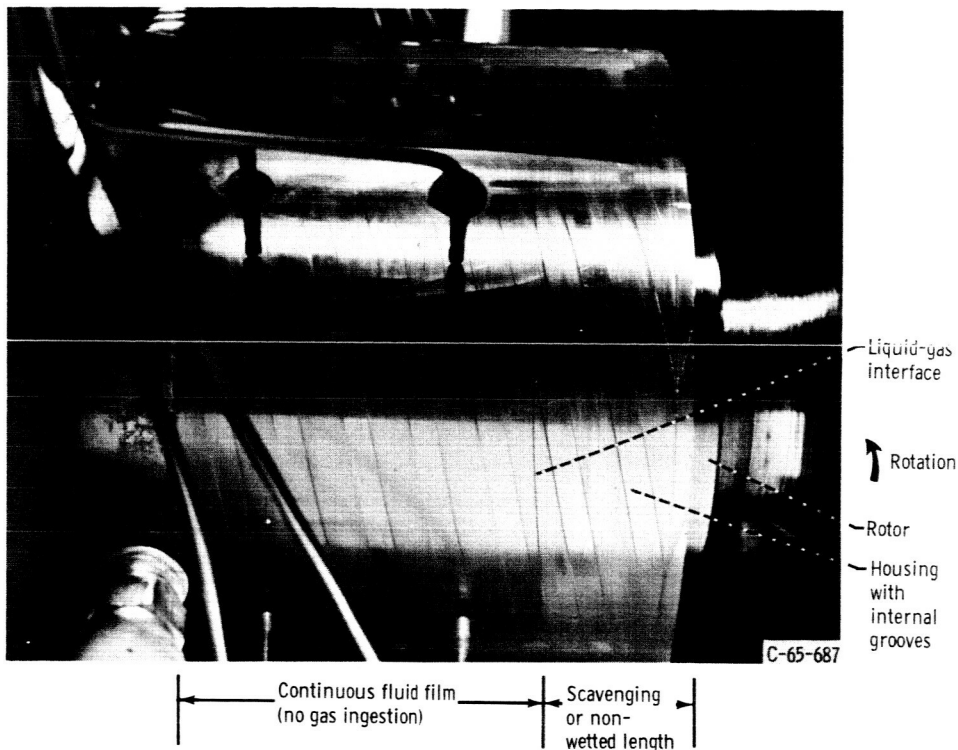


(a) Rotational speed, 1000 rpm; average temperature of oil film,  $97^{\circ}\text{F}$ ; temperature change along oil film,  $11^{\circ}\text{F}$ ; cavity pressure, 54.1 lb/sq in. absolute.

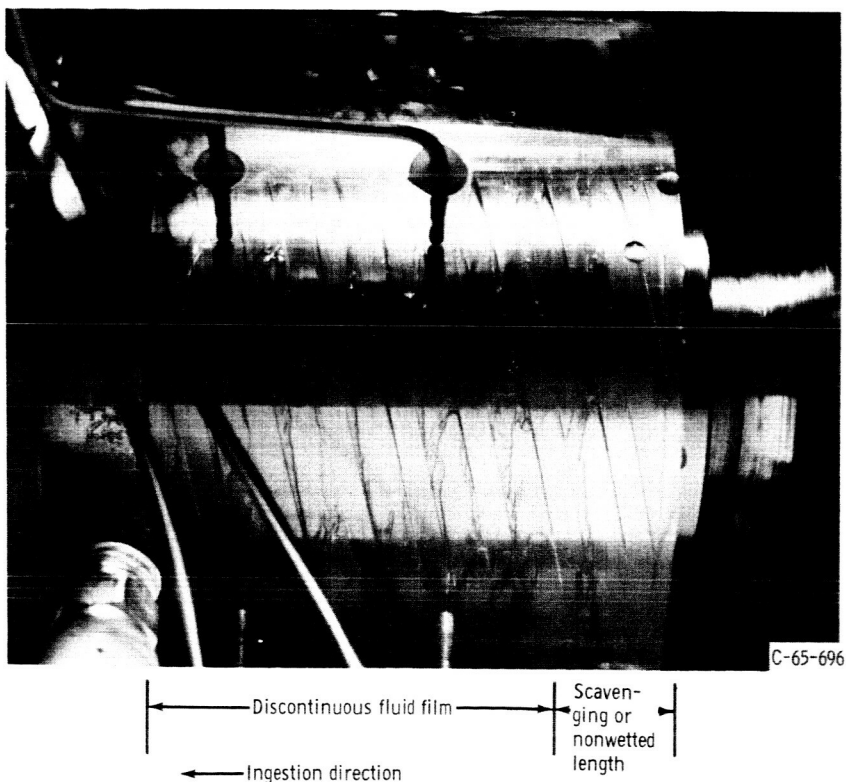


(b) Rotational speed, 6000 rpm; average temperature of oil film,  $132^{\circ}\text{F}$ ; temperature change along oil film,  $19^{\circ}\text{F}$ ; cavity pressure, 80.6 lb/sq in. absolute.

Figure 8. - Axial pressure gradients near helical groove edges with grooves in direct communication with pressurized cavity.

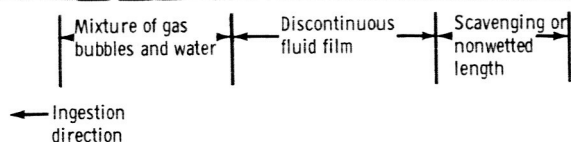
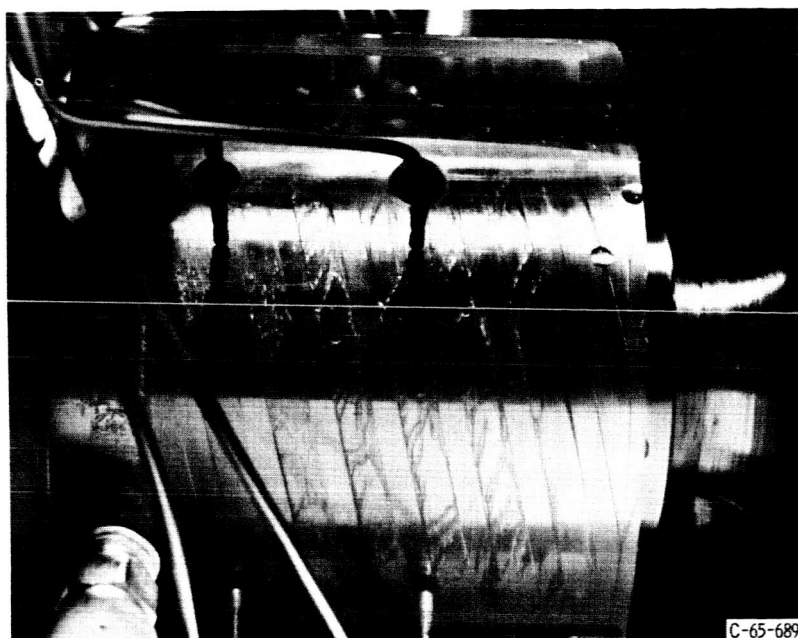
High-  
pressure  
end

(a) Modified Reynolds number, 1.75 (2000 rpm).

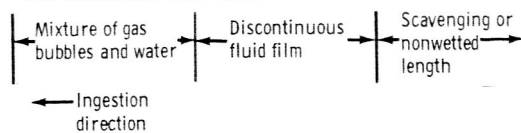
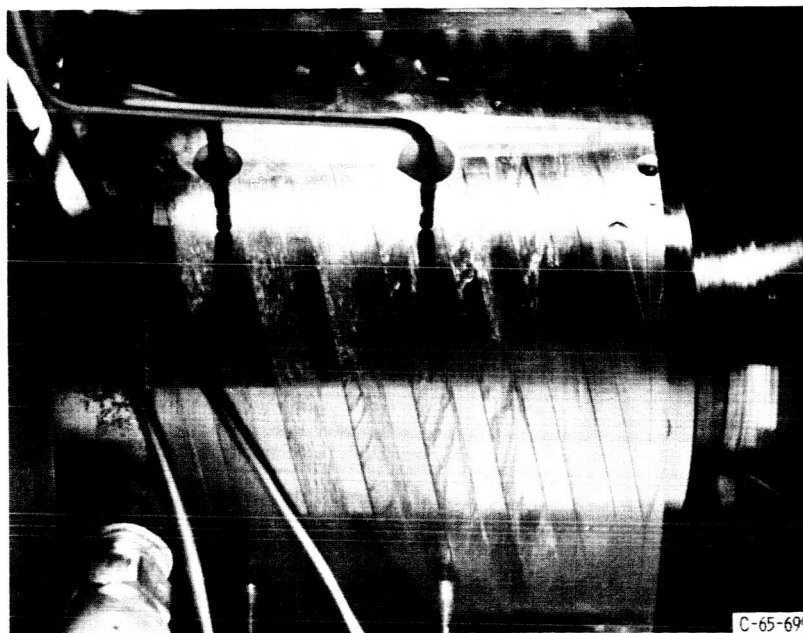
High-  
pressure  
end

(b) Modified Reynolds number, 2.58 (3000 rpm).

Figure 9. - Grooved housing viscoseal operation when sealing water.

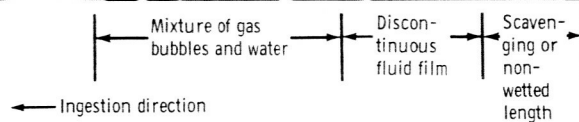
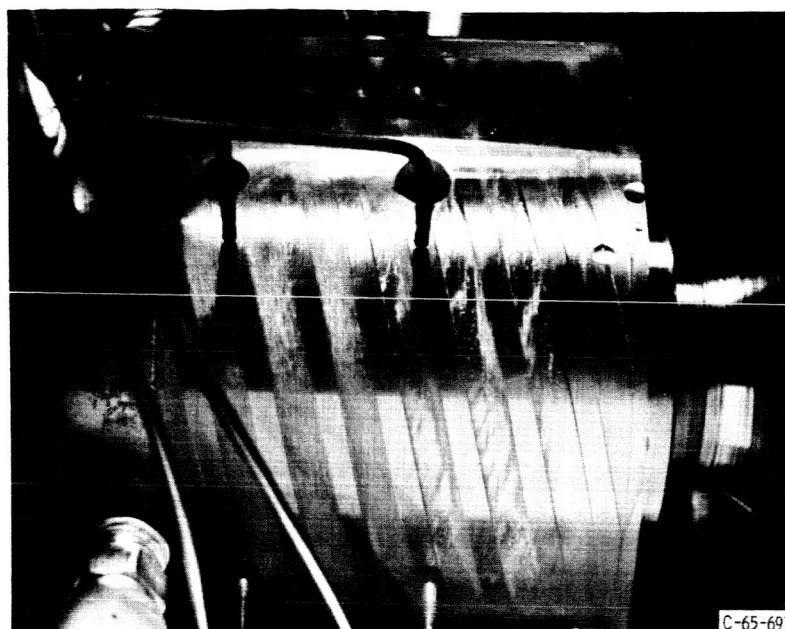
High-  
pressure  
end

(c) Modified Reynolds number, 3.50 (4000 rpm).

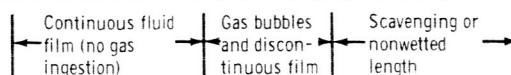
High-  
pressure  
end

(d) Modified Reynolds number, 4.42 (5000 rpm).

Figure 9. - Continued.

High-  
pressure  
end

(e) Modified Reynolds number, 5.25 (6000 rpm).

High-  
pressure  
end

(f) Modified Reynolds number, 7.00 (8000 rpm).

Figure 9. - Concluded.

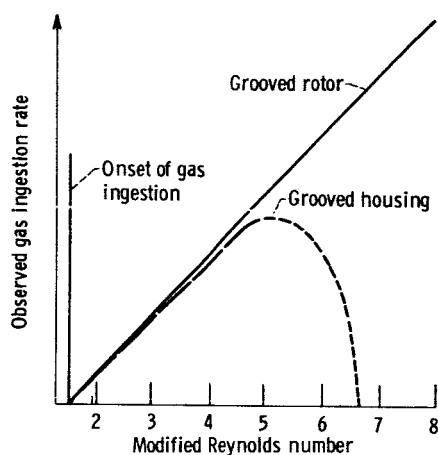


Figure 10. - Comparison of observed gas ingestion when sealing water for grooved housing and grooved rotor viscoseals.

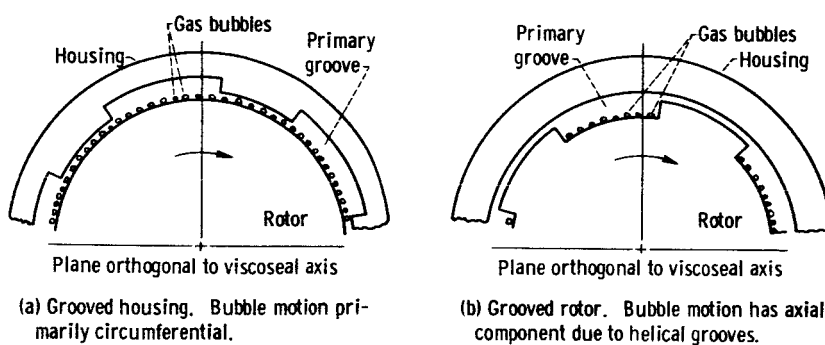
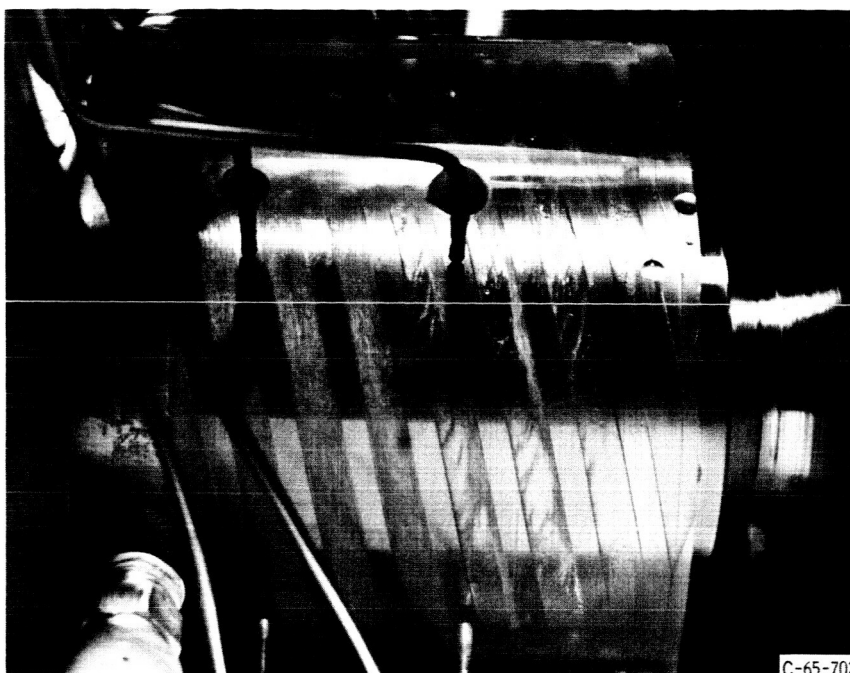


Figure 11. - Gas ingestion mechanisms of grooved housing compared with grooved rotor viscoseal.

High-pressure end



C-65-702

← Gas ingestion direction and increasing liquid-gas density

No leakage at low-pressure end

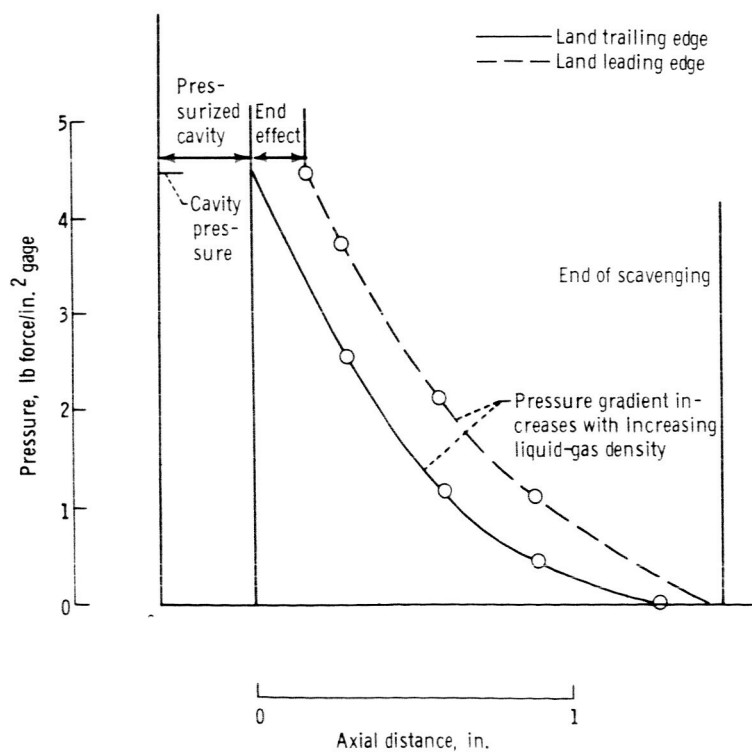


Figure 12. - Pressure as function of axial length with gas ingestion for grooved rotor. Sealed fluid, water.

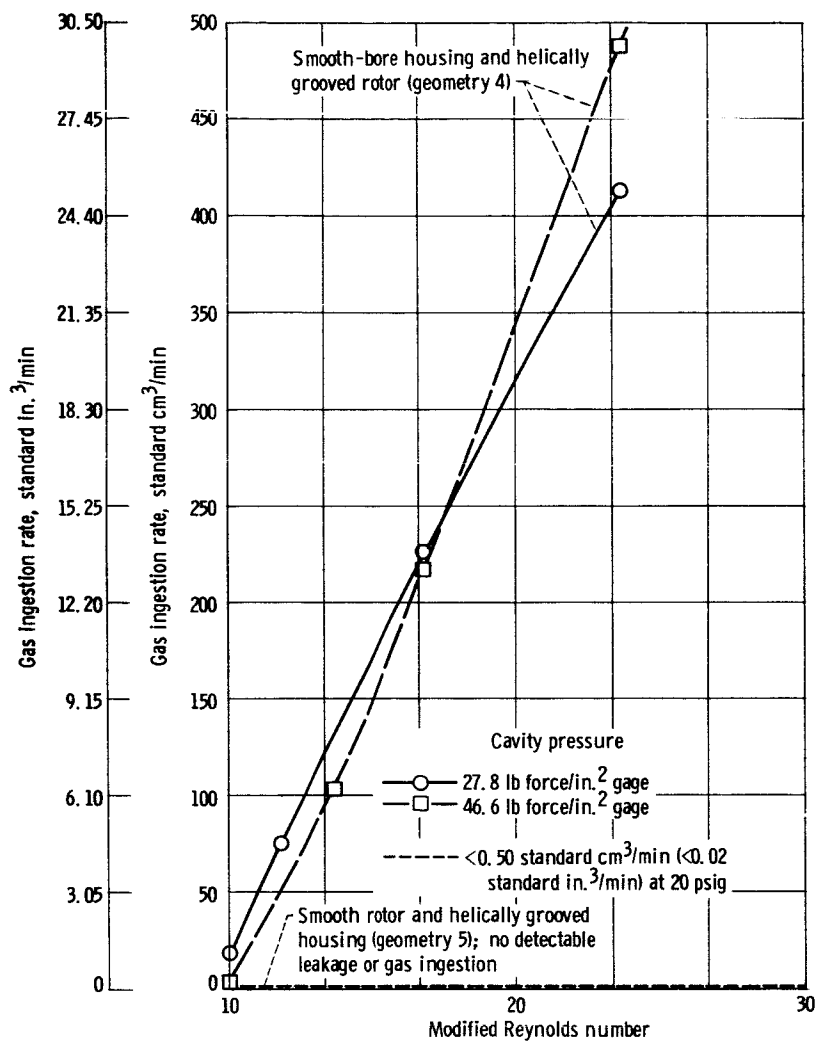
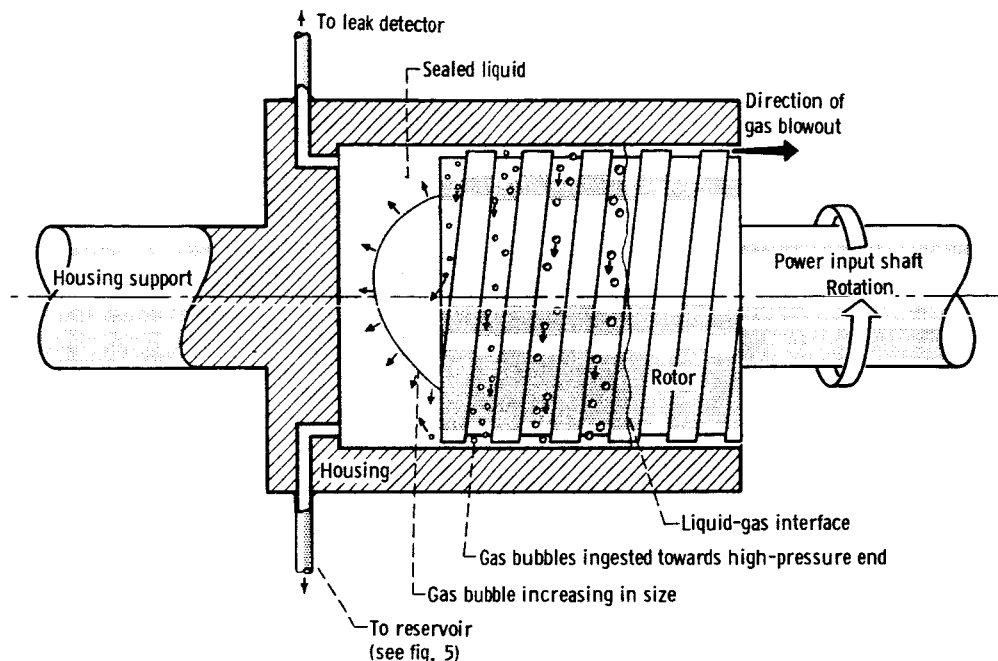
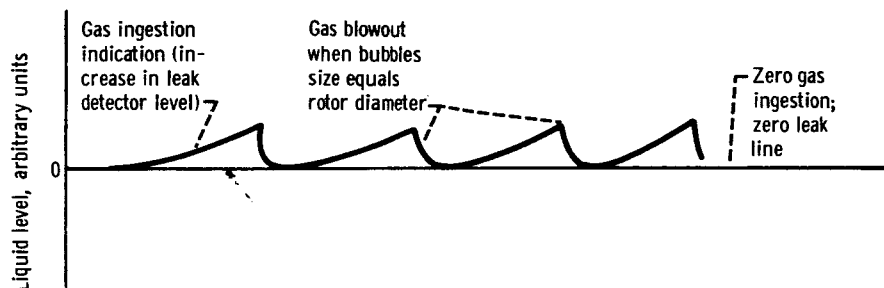


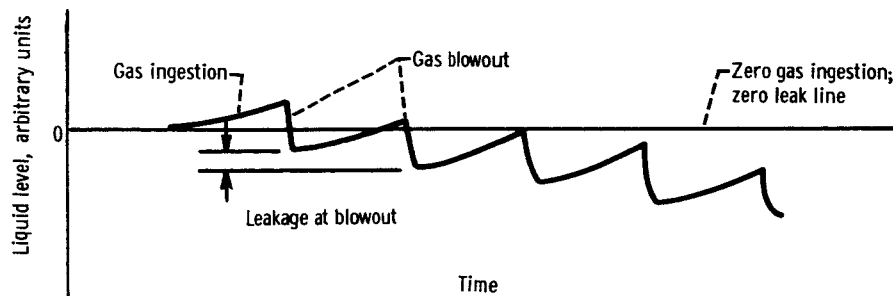
Figure 13. - Gas ingestion rate when sealing liquid sodium at 400° F.



(a) Mechanism involved in gas ingestion into pressurized cavity.



(b) Schematic liquid level oscillograph trace for repeated cycles of gas ingestion, subsequent gas blowout, and no liquid leakage at blowout.



(c) Schematic liquid level oscillograph trace for repeated cycles of gas ingestion, subsequent gas blowout, and liquid leakage at blowout.

Figure 14. - Gas ingestion into closed cavity.



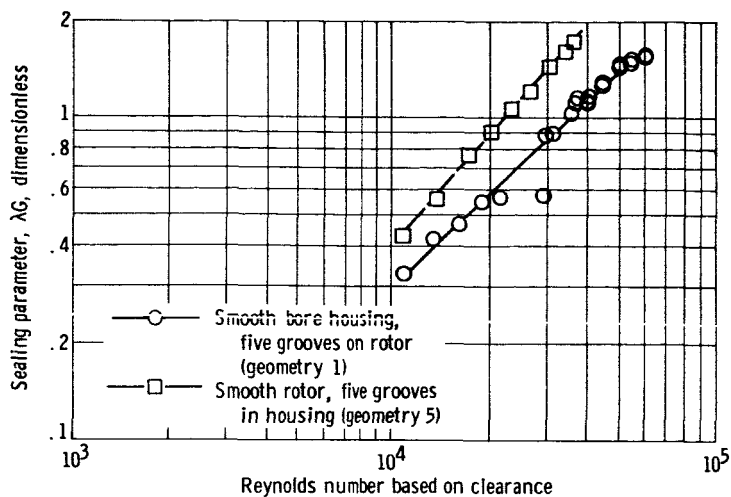


Figure 15. - Comparison of sealing parameters for grooved rotor and housing operating in sodium. Sodium temperature, 165° to 335° C (329° to 635° F).

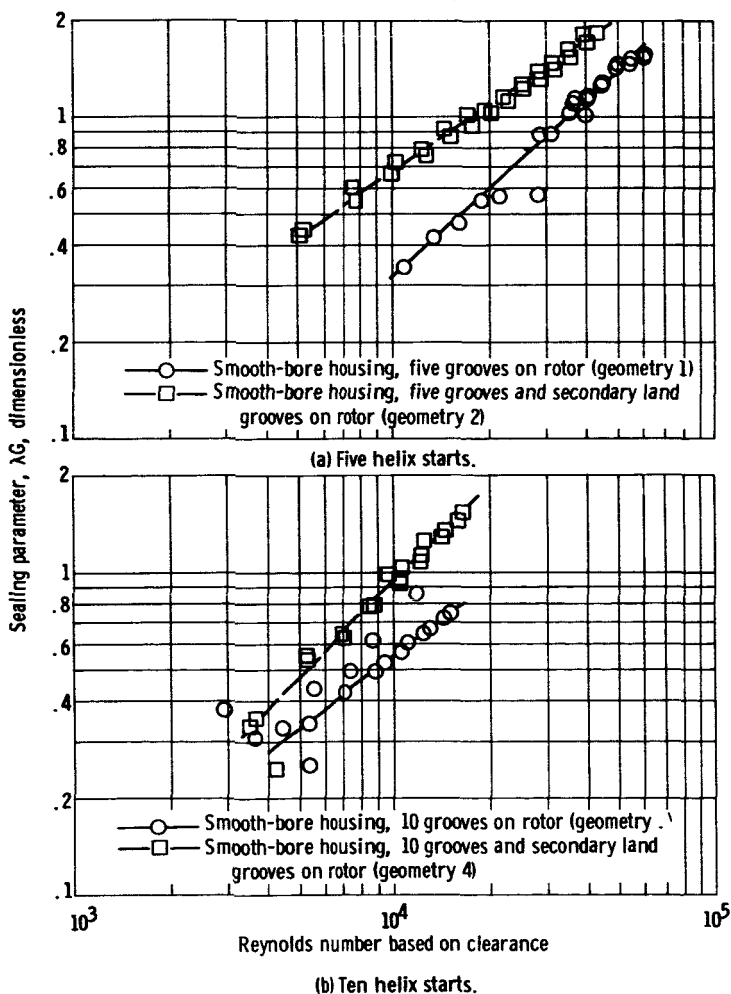
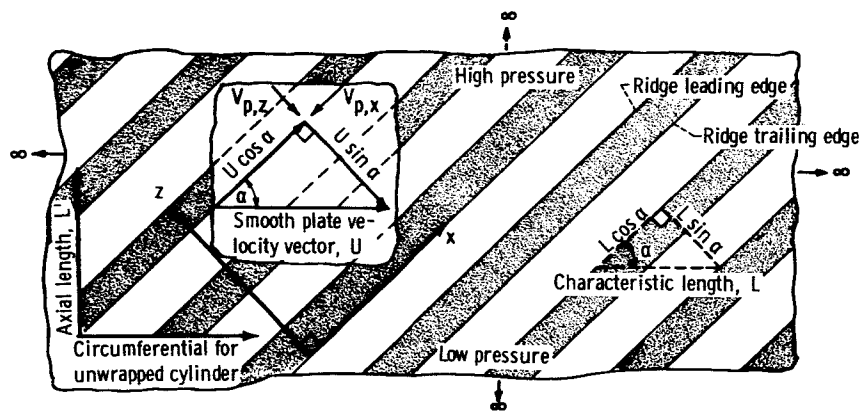
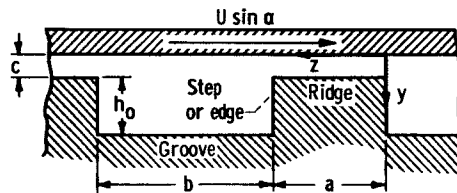


Figure 16. - Comparison of sealing parameter obtained with helically grooved rotor with and without secondary land grooves operating in sodium. Sodium temperature, 165° to 335° C (329° to 635° F).

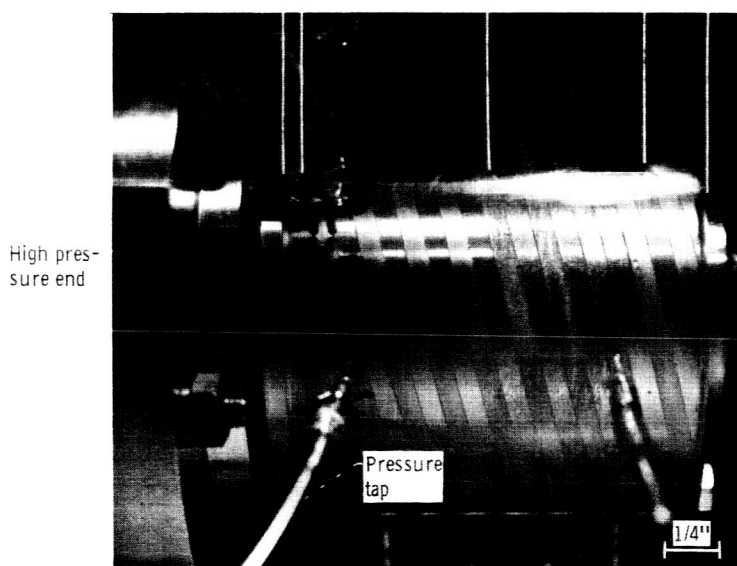
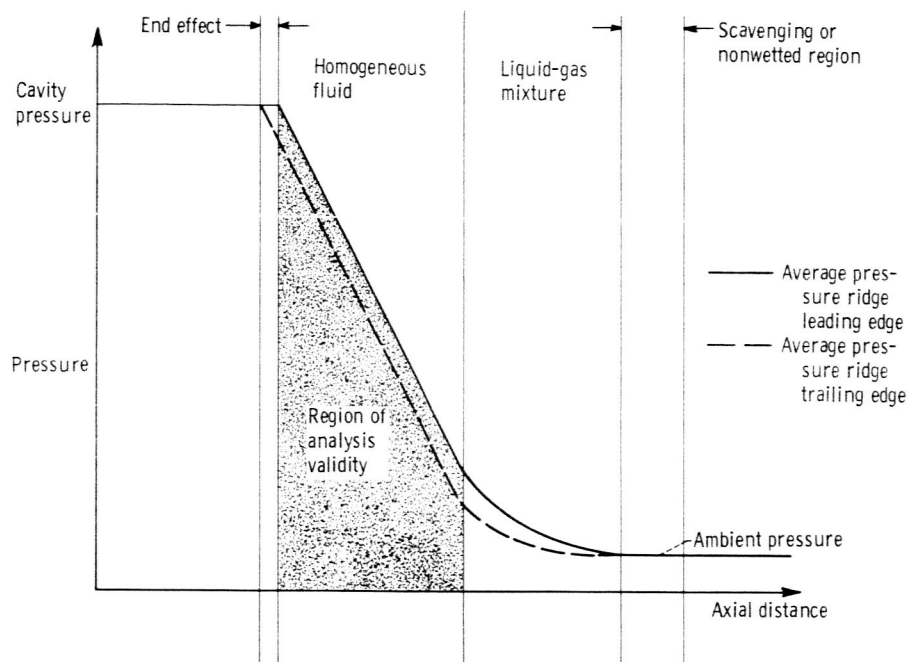


(a) Plan view.



(b) Cross-sectional view along z-axis illustrating relative motion of smooth flat plate with respect to fixed parallel groove-ridge plate.

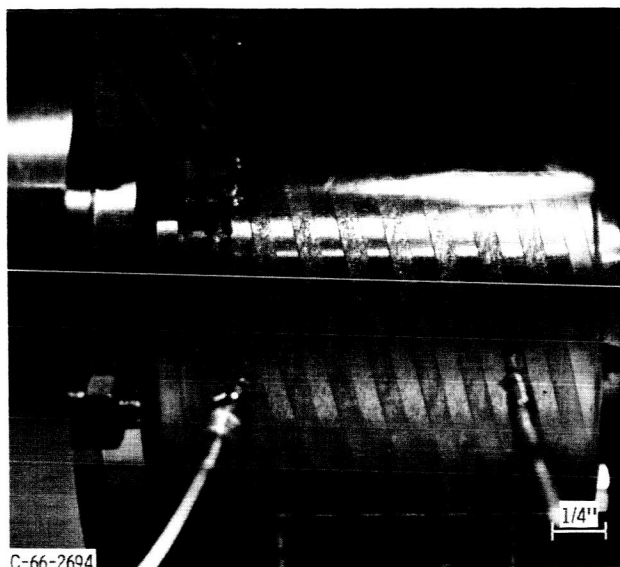
Figure 17. - Mathematical model of parallel groove-ridge geometry of infinite horizontal extent.



C-66-2693

Figure 18. - Region of analysis validity (homogeneous fluid) of a grooved housing viscoseal. Reynolds number based on clearance or film thickness, 1700; modified or reduced Reynolds number, 19; 400-microinch shaft rotational movement during photographic exposure; shaft speed, 8000 rpm; sealed fluid, water.

High pressure end



Discontinuous fluid film  
(mixed air and liquid)

Figure 19. - Viscoseal with grooved housing operating in a regime of water-air mixture (gas ingestion). Analyses does not apply for this discontinuous fluid film case; 250-microinch shaft rotational movement during photographic exposure; shaft speed, 5000 rpm; sealed fluid, water.

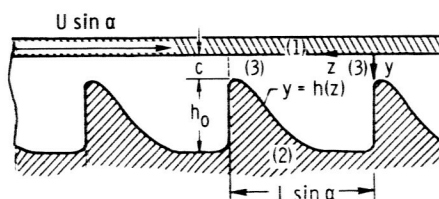


Figure 20. - Cross-sectional view along  $z$ -axis illustrating arbitrary groove-ridge pair shape.

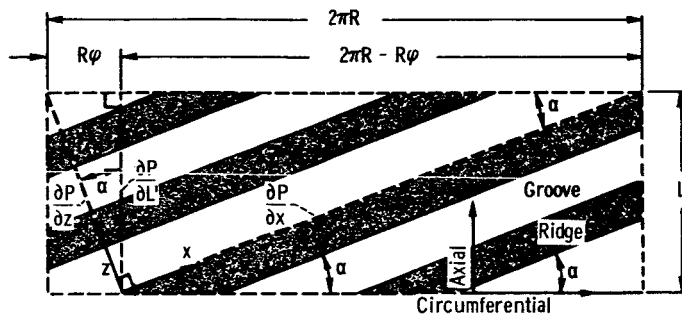


Figure 21. - Resolution of across and along groove-ridge pressure gradients into axial pressure gradient. "Unwrapped" cylinder is shown.

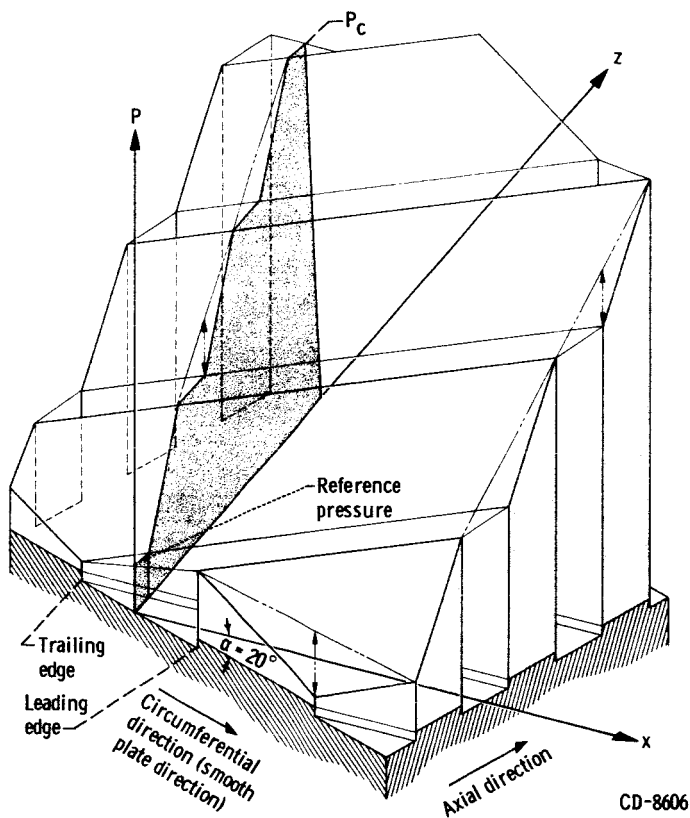
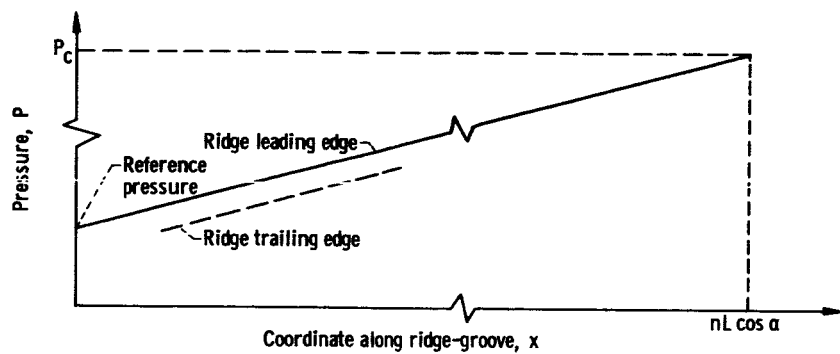
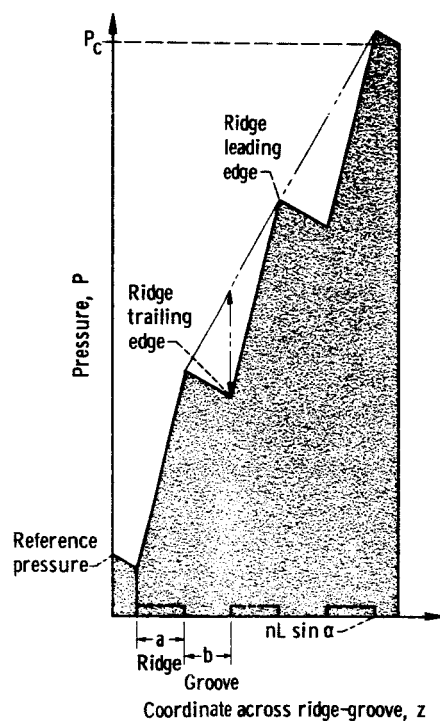


Figure 22. - Pressure distribution over parallel groove geometry. (Qualitative graphical representation from experimental data.)

CD-8606



(a) Along ridges or grooves (no end effects are shown).



(b) Across ridges and grooves (no restriction that profile must be linear).

Figure 23. - Pressure profiles (qualitative graphical representation from experimental data).

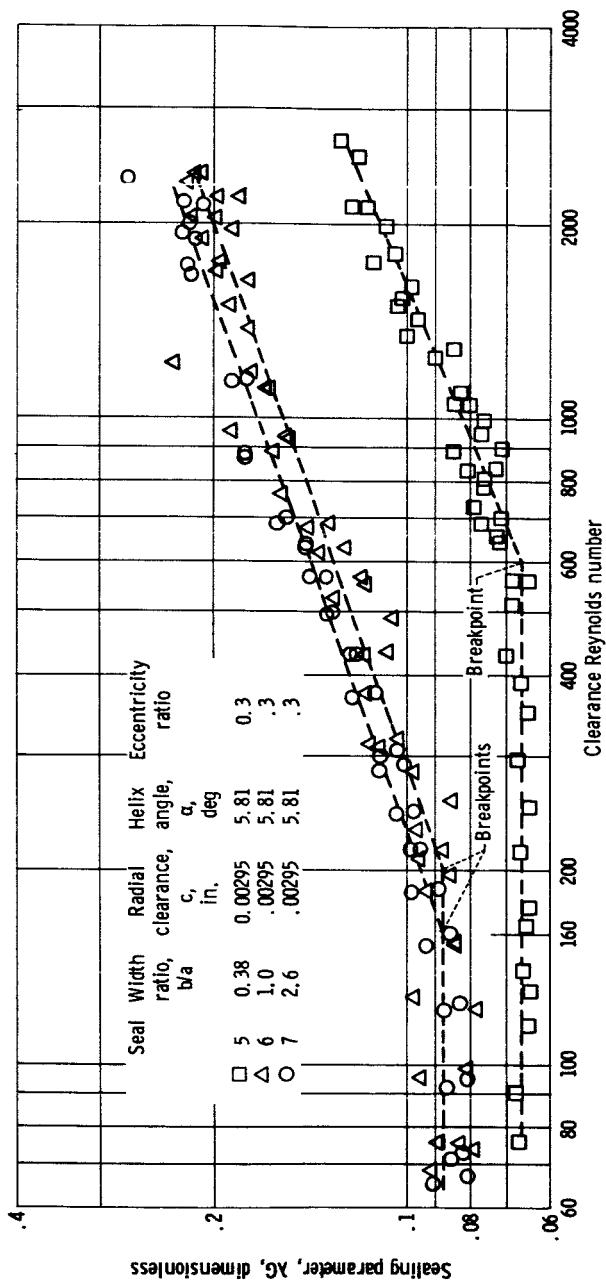


Figure 24. - Experimental sealing parameter for seals 5, 6, and 7 from reference 27.

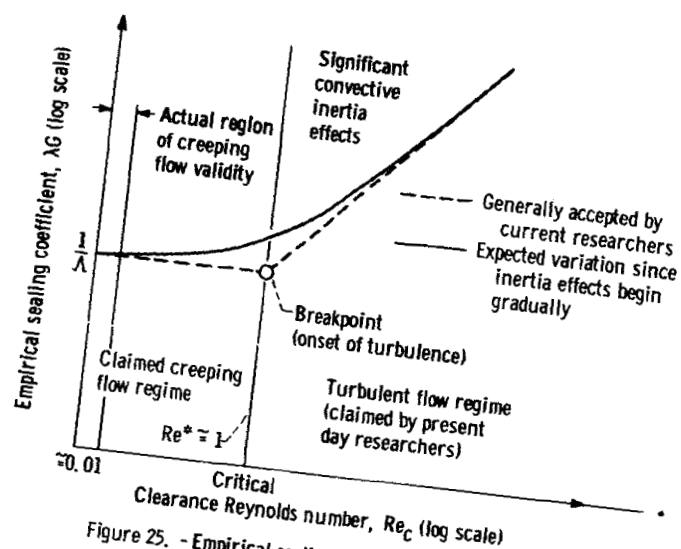


Figure 25. - Empirical sealing coefficient as function of clearance Reynolds number.

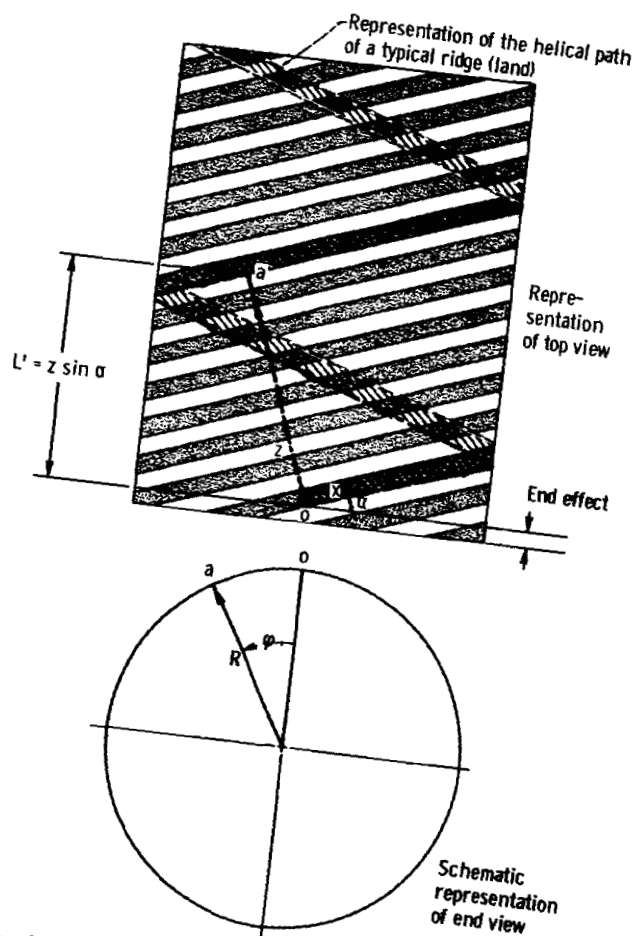


Figure 26. - Illustration that a point on the viscoseal surface can be reached from the origin axis along both the  $x = \text{constant}$  and  $z = \text{constant}$  surface coordinate paths (for example, paths from  $o$  to  $a$ ).



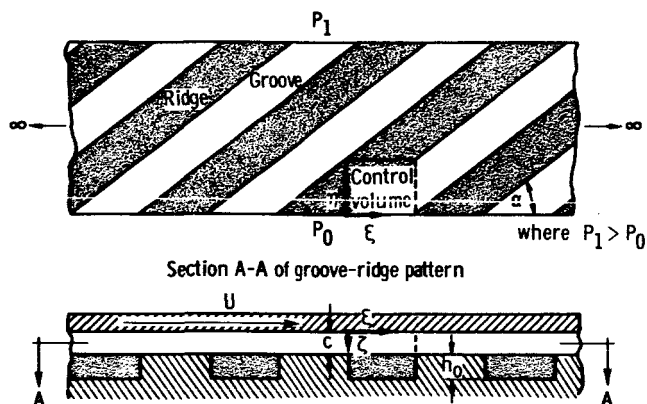


Figure 27. - Model used in creeping flow solution.

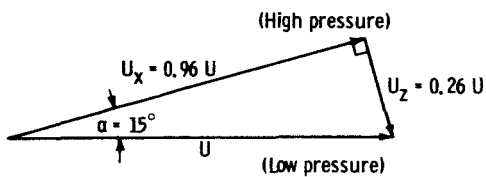
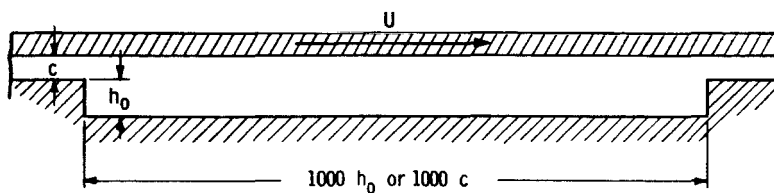


Figure 28. - Resolution of plate velocity (or drag force) into components along and across groove or ridge.

Figure 29. - Example where the creeping flow mathematical model can be considered a valid physical model. Modified Reynolds number ( $Re^*$ ) much less than 1 since clearance  $c$  is much less than characteristic length  $L$ .